

A systematic study of silicate absorption features in heavily obscured AGNs observed by Spitzer/IRS

T. Tsuchikawa,¹ H. Kaneda,¹ S. Oyabu,² T. Kokusho,¹ H. Kobayashi,¹ M. Yamagishi³ and Y. Toba^{4,5,6}

¹ Graduate School of Science, Nagoya University, Furo-cho, Chikusa-ku, Nagoya, Aichi 464-8602, Japan
e-mail: tsuchikawa@u.phys.nagoya-u.ac.jp

² Institute of Liberal Arts and Sciences, Tokushima University, 1-1 Minami-Jyosanjima, Tokushima-shi, Tokushima, 770-8502, Japan

³ Institute of Space and Astronautical Science, Japan Aerospace Exploration Agency, 3-1-1 Yoshinodai, Chuo-ku, Sagami-hara, Kanagawa, 252-5210, Japan

⁴ Department of Astronomy, Kyoto University, Kitashirakawa-Oiwake-cho, Sakyo-ku, Kyoto 606-8502, Japan

⁵ Academia Sinica Institute of Astronomy and Astrophysics, 11F of Astronomy-Mathematics Building, AS/NTU, No.1, Section 4, Roosevelt Road, Taipei 10617, Taiwan

⁶ Research Center for Space and Cosmic Evolution, Ehime University, 2-5 Bunkyo-cho, Matsuyama, Ehime 790-8577, Japan

Received February 3, 2021; accepted May 10, 2021

ABSTRACT

Context. Heavily obscured active galactic nuclei (AGNs) are known to show deep silicate absorption features in the mid-infrared (IR) wavelength range of 10–20 μm . The detailed profiles of the features reflect the properties of silicate dust, which are likely to include information on AGN activities obscured by large amounts of dust.

Aims. We reveal AGN activities obscured by large amounts of dust through the silicate dust properties obtained from the mid-IR spectral bands.

Methods. We select 115 mid-IR spectra of heavily obscured AGNs observed by Spitzer/IRS, and systematically analyze the composition of silicate dust by spectral fitting using the 10 μm amorphous and 23 μm crystalline bands.

Results. We find that the main component of the silicate dust obscuring AGNs is amorphous olivine, the median mass column density of which is one order of magnitude higher than those of the minor components of amorphous pyroxene and crystalline forsterite. The median mass fraction of the amorphous pyroxene, $\sim 2\%$, is significantly lower than that of the diffuse interstellar medium (ISM) dust in our Galaxy, while the median mass fraction of the crystalline forsterite, $\sim 6\%$, is higher than that of the diffuse ISM dust. We also find that the mass fractions of the amorphous pyroxene and the crystalline forsterite positively correlate with each other.

Conclusions. The low mass fraction of the amorphous pyroxene suggests that the obscuring silicate dust is newly formed, originating from starburst activities. The relatively high mass fraction of crystalline forsterite implies that the silicate dust is processed in the high temperature environment close to the nucleus and transported to outer cooler regions by molecular outflows. The positive correlation between the mass fractions can be naturally explained considering that amorphous pyroxene is transformed from crystalline forsterite by ion bombardments. We also find that spectra with high ratios of the H₂O ice absorption to silicate mass column density tend to indicate low mass fractions of amorphous pyroxene and crystalline forsterite, which is consistent with the scenario of the thermal dust processing close to the nucleus.

Key words. dust, extinction – Infrared: galaxies – galaxies: nuclei

1. Introduction

The central engine of an active galactic nucleus (AGN) is considered to be surrounded by thick gas and dust, which have a toroidal structure predicted by the classical unified model (Antonucci 1993; Urry & Padovani 1995). Near- to mid-infrared (IR) and hard X-ray observations over the last two decades have revealed the existence of a lot of galaxies harboring AGNs despite no optical signatures of AGN (e.g., Imanishi & Dudley 2000; Risaliti et al. 2000). The hidden AGNs are heavily obscured by such dense gas and dust that ionizing photons cannot escape from the nuclear region, and thus narrow line region (NLR), which is an ionized polar region emitting optical lines, is considered not to be developed (e.g., Imanishi et al. 2006). The standard supermassive black hole (SMBH) and galaxy co-evolutionary scenario predicts that heavily obscured AGNs are in an early phase of the SMBH growth (Hopkins et al. 2008). Therefore, in order to understand the AGN evolution, it is impor-

tant to study the nature of the heavily obscured AGN activities and the obscuring material.

Amorphous silicate is a major component of the interstellar dust (Mathis et al. 1977), the band features of which peak at the mid-IR wavelengths of ~ 10 and ~ 18 μm in Si-O stretching and O-Si-O bending modes, respectively. These bands with the absolute value of the silicate strength > 1 are seen in 97 out of 196 mid-IR spectra of nearby AGNs and ultra-luminous IR galaxies (ULIRGs) (Hao et al. 2007). In particular, owing to the large samples observed by Spitzer/IRS (Houck et al. 2004), mid-IR properties of low-redshift AGNs ($z < 1$) have been studied well (e.g., Weedman et al. 2005; Hao et al. 2007; Imanishi et al. 2007; Spoon et al. 2007). In these studies, the strengths of the silicate features at the peak wavelengths were often analyzed, from which it was found that the silicate features in QSOs or type-1 AGNs are observed in emission or weak absorption, while those in type-2 AGNs only in absorption (e.g., Hao et al. 2007; Spoon et al. 2007; Hatziminaoglou et al. 2015). The silicate features in

heavily obscured AGNs tend to show deep absorption, the optical depths of which are greater than 2 (e.g., Hao et al. 2007; Imanishi et al. 2007). In general, the strengths of the silicate features depend on the geometrical structure of obscuring clouds along the line of sight, while their profile shapes reflect the dust properties, such as chemical composition and crystallinity (Henning 2010). For example, the peaks of the 10 μm silicate emission features in the spectra of QSOs and type-1 AGNs are known to shift toward longer wavelengths than that of typical amorphous silicate, which is explained by higher porosity (Li et al. 2008), a larger size of dust (Smith et al. 2010), or other dust components (Markwick-Kemper et al. 2007; Srinivasan et al. 2017).

In the Circinus galaxy, a famous type-2 AGN, crystalline silicate is detected with ground-based telescopes, showing that the crystallinity is similar to that of the diffuse interstellar medium (ISM) silicate in our Galaxy (Duy & Lawson 2019). On the other hand, Spoon et al. (2006) find that 12 ULIRGs with deep silicate absorption features in the mid-IR spectra have silicate dust with crystallinity higher than the diffuse ISM silicate dust in our Galaxy. Spoon et al. (2006) suggest that the high crystallinity originates from starburst activities, while Kemper et al. (2011) predict that the high crystallinity nature needs an additional source producing crystalline silicate other than starburst activities.

Tsuchikawa et al. (2019) investigate the profile shapes of the 10 μm silicate features in 39 heavily obscured AGNs observed by AKARI/IRC and Spitzer/IRS, and find that the profile shapes are notably similar as a whole. Nevertheless, they also find that the profile shapes are different in the wing on the shorter wavelength side, which indicates the variation of the mineralogical composition of silicate dust from galaxy to galaxy. In this paper, we systematically quantify the detailed differences in the silicate features in heavily obscured AGNs, and determine the dust properties for each galaxy. Using the dust properties thus obtained, we aim to reveal obscured AGN activities and the surrounding environments.

2. Sample selection

We use mid-IR spectra observed by the Infrared Spectrograph (IRS; Houck et al. 2004) aboard the Spitzer Space Telescope (Werner et al. 2004). IRS low-resolution (LR) spectra were observed using two spectroscopic modules (Short-Low; SL, Long-Low; LL), covering the wavelength ranges of 5.2–14.5 and 14.0–38.0 μm , and therefore we can study both the silicate 10 and 18 μm features for low-redshift galaxies. The spectroscopic data were retrieved from the Cornell AtlaS of Spitzer/IRS Sources (CASSIS; Lebouteiller et al. 2011, 2015) version LR7 which contain more than 10,000 LR spectra. The CASSIS provides the spectra reduced by the two spectral extraction techniques which are the optimal extraction for point-like sources and the tapered column extraction for partially-extended sources. We selected either of the two spectral extraction methods for each spectrum according to the pipeline message based on the source spatial extent. Most of the spectra retrieved from CASSIS show discontinuity in the flux density between the SL and LL spectra, which is mainly caused by difference in the extraction aperture and slit width between the SL and LL modules, and thus we performed a spectral stitching by scaling the SL spectra.

Among the spectra of extragalactic sources in CASSIS, which we searched for according to the science category of the approved Spitzer programs, we retrieved those with apparently deep silicate absorption features. We selected 115 obscured AGNs using the following three selection criteria from the sam-

ple retrieved from CASSIS: (1) the apparent peak optical depth of the 10 μm silicate feature is larger than 1.5. The apparent peak optical depth is defined by $-\ln(f_{\text{obs}}(10 \mu\text{m})/f_{\text{cont}}(10 \mu\text{m}))$, where $f_{\text{obs}}(10 \mu\text{m})$ and $f_{\text{cont}}(10 \mu\text{m})$ are an observed flux density and absorption-free continuum flux density, respectively, both at the peak wavelength of the 10 μm silicate feature (Spoon et al. 2007). The absorption-free continuum is assumed to be the power-law function determined from the flux densities at 7.1 and 14.2 μm , following the method defined by e.g., Imanishi et al. (2007). Since some spectra showed low signal-to-noise ratios (S/N) at the bottom of the 10 μm silicate feature, we performed spectral binning so that S/N at 10 μm exceeded 5, and then calculated the apparent optical depth of the 10 μm silicate feature at the peak wavelength. (2) The equivalent width of the polycyclic aromatic hydrocarbon (PAH) 6.2 μm feature is smaller than 270 nm, by which we can select AGN-dominated galaxies (Stierwalt et al. 2013). We calculated the equivalent width by integrating the flux densities above the power-law local continuum determined from the flux densities at 6.0 and 6.45 μm (e.g., Imanishi et al. 2007). By this criterion, we analyze the silicate features robustly with less contamination of the PAH emission. Fifty one sources which meet criteria (1) and (3) are removed out of 166 based on criterion (2). (3) The redshift z is lower than 0.35. The spectra of low-redshift galaxies selected by the criterion cover both silicate 10 and 18 μm features. Table 1 summarizes the general properties of the 115 obscured AGNs selected by the above three criteria. Although IRAS 13454–2956N, WISEA 142500.11+325949.9 and WISEA J231813.00–004125.9 meet all the three selection criteria, we excluded them from our sample because the spectral data of one of the orders in the LR module are not available. IRAS 16255+2801 is confused with a planetary nebula in our Galaxy, and hence also excluded from our sample.

3. Spectral decomposition of the 10 μm silicate feature

3.1. Mid-IR spectral modeling

In order to investigate the dust properties, we decompose the 10 μm silicate feature in our sample by spectral fitting in the wavelength range of 5.3–12 μm , where we assume the screen geometry for simplicity. The fitting function, F_ν , is described as

$$F_\nu = F_{\text{hot,AGN}} \exp(-\tau_{\text{sil}} - \tau_{\text{ice+HAC}}) + F_{\text{PAH}} + F_{\text{line}} + F_{\text{hot,unobs}}, \quad (1)$$

where $F_{\text{hot,AGN}}$, F_{PAH} , F_{line} and $F_{\text{hot,unobs}}$ are the absorption-free continuum emission due to the hot dust heated by AGN, PAH and line emissions and an additional continuum emission due to unobscured hot dust, respectively. τ_{sil} and $\tau_{\text{ice+HAC}}$ are the optical depths of silicate dust and water ice plus hydrogenated amorphous carbon (HAC).

In the spectral fitting, we have to accurately determine $F_{\text{hot,AGN}}$ to extract the properties of silicate dust. Tsuchikawa et al. (2019) reproduced the 2.5–12.5 μm spectrum of the heavily obscured AGN LEDA 1712304 well by a single-temperature blackbody emission as an absorption-free continuum, while the spectra in our sample are expected to be poorly fitted by the same model as used in Tsuchikawa et al. (2019) due to the variety of the spectra. Spoon et al. (2006) adopted the spline continuum using the pivot points anchored at the wavelengths of 5.6, 7.1 μm and the longer wavelength end of the spectra, and, for feature-less spectra, replaced the anchor point at 7.1 μm by the continuum at 7.9–8.0 μm . The method can be considered as good estimates for feature-less spectra as shown in figure 1 of

Table 1. General properties of our sample

Name (1)	AORkey (2)	R.A. (J2000) (3)	Dec. (J2000) (4)	z (5)
IRAS 00091-0738	10440960, 10108928	00h11m43.2s	-07d22m06s	0.1184
IRAS F00183-7111	7556352	00h20m34.6s	-70d55m26s	0.3270
IRAS 00188-0856	4962560	00h21m26.4s	-08d39m27s	0.1284
IRAS 00397-1312	4963584	00h42m15.4s	-12d56m03s	0.2617
IRAS 00406-3127	4964096	00h43m03.1s	-31d10m49s	0.3424
IRAS 01166-0844SE	10441984, 10109952	01h19m07.8s	-08d29m12s	0.1180
IRAS F01173+1405	20356352	01h20m02.6s	+14d21m42s	0.0312
IRAS F01197+0044	22132224	01h22m18.1s	+01d00m25s	0.0555
IRAS 01199-2307	4964864	01h22m20.8s	-22d51m57s	0.1562
IRAS 01298-0744	4965120	01h32m21.4s	-07d29m08s	0.1362
IRAS 01355-1814	4965376	01h37m57.4s	-17d59m20s	0.1920
IRAS F01478+1254	23012864	01h50m28.4s	+13d08m58s	0.1470
IRAS 01569-2939	10110208	01h59m13.7s	-29d24m34s	0.1400
IRAS 02438+2122	10508544, 20353792	02h46m39.1s	+21d35m10s	0.0233
IRAS 02455-2220	4967680	02h47m51.2s	-22d07m38s	0.2840
IRAS 02530+0211	6652160	02h55m34.4s	+02d23m41s	0.0276
IRAS 03158+4227	12256256	03h19m11.9s	+42d38m25s	0.1344
NGC 1377 ^a	9511424	03h36m40.1s	-20d54m02s	0.0060
IRAS 03538-6432	4968192	03h54m25.2s	-64d23m44s	0.3007
IRAS 03582+6012	20341504	04h02m32.9s	+60d20m41s	0.0300
IRAS 04074-2801	25185536	04h09m30.4s	-27d53m43s	0.1537
IRAS 04313-1649	4968960	04h33m37.0s	-16d43m31s	0.2680
IRAS 04384-4848	6650880	04h39m50.8s	-48d43m17s	0.2035
ESO 203-IG001	20334080	04h46m49.5s	-48d33m30s	0.0529
IRAS 05020-2941	25185792	05h04m00.7s	-29d36m54s	0.1544
IRAS F06076-2139	20359680	06h09m45.7s	-21d40m24s	0.0374
IRAS 06206-6315	4969984	06h21m00.8s	-63d17m23s	0.0924
IRAS 06301-7934	4970240	06h26m42.2s	-79d36m30s	0.1564
IRAS 06361-6217	4970496	06h36m35.7s	-62d20m31s	0.1596
IRAS F07224+3003	19165184	07h25m37.2s	+29d57m14s	0.0188
IRAS 07251-0248	20346112	07h27m37.6s	-02d54m54s	0.0876
MCG +02-20-003	20353280	07h35m43.4s	+11d42m34s	0.0163
SDSS J082001.72+505039.1	23014400	08h20m01.7s	+50d50m39s	0.2173
IRAS 08201+2801	18202112	08h23m12.6s	+27d51m40s	0.1678
IRAS F08520-6850	20343808	08h52m32.0s	-69d01m54s	0.0451
IRAS 08572+3915	4972032	09h00m25.3s	+39d03m54s	0.0584
IRAS 09039+0503	10443776, 10104064	09h06m34.0s	+04d51m25s	0.1251
IRAS 09539+0857	10444032, 11676160	09h56m34.3s	+08d43m05s	0.1289
IRAS F10038-3338	20352256	10h06m04.6s	-33d53m06s	0.0342
IRAS 10091+4704	4973824	10h12m16.7s	+46d49m42s	0.2460
IRAS F10112-0040	15069440	10h13m46.8s	-00d54m51s	0.0425
IRAS 10173+0828	14838528, 20314880	10h20m00.2s	+08d13m34s	0.0491
IRAS F10237+4720	22117632	10h26m48.2s	+47d05m07s	0.0589
IRAS 10378+1109	4974336	10h40m29.1s	+10d53m17s	0.1363
IRAS 10485-1447	10444800, 10105088	10h51m03.0s	-15d03m22s	0.1330
IRAS 11028+3130	18203392	11h05m37.5s	+31d14m31s	0.1986
IRAS 11038+3217	4975104	11h06m35.7s	+32d01m46s	0.1300
IRAS 11095-0238	4975360	11h12m03.3s	-02d54m24s	0.1066
IRAS 11130-2659	10105600	11h15m31.5s	-27d16m22s	0.1361
IRAS 11180+1623	18203648	11h20m41.7s	+16d06m56s	0.1660
IRAS 11223-1244	4976128	11h24m50.7s	-13d01m16s	0.1990
IRAS 11506+1331	10445312, 10111488	11h53m14.1s	+13d14m26s	0.1273
IRAS 11524+1058	18203904	11h55m05.1s	+10d41m22s	0.1787
IRAS 11582+3020	4976384	12h00m46.8s	+30d04m14s	0.2230
IRAS 12032+1707	4976896	12h05m47.7s	+16d51m08s	0.2178
IRAS 12127-1412	10445824, 10105856	12h15m19.1s	-14d29m41s	0.1330
IRAS F12224-0624	20367104	12h25m03.9s	-06d40m52s	0.0264
NGC 4418	4935168	12h26m54.6s	-00d52m40s	0.0073
IRAS 12359-0725	10106112	12h38m31.6s	-07d42m25s	0.1380
IRAS 12447+3721	25187840	12h47m07.7s	+37d05m36s	0.1580
IRAS F13045+2354	4168448	13h07m00.6s	+23d38m04s	0.2750

Table 1. Continued.

Name (1)	AORkey (2)	R.A. (J2000) (3)	Dec. (J2000) (4)	z (5)
IRAS 13106-0922	25186048	13h13m14.6s	-09d38m08s	0.1745
IRAS F13279+3401	12235264	13h30m15.2s	+33d46m29s	0.0230
IRAS 13352+6402	4979968	13h36m51.1s	+63d47m04s	0.2366
Mrk 273	4980224	13h44m42.1s	+55d53m13s	0.0378
IRAS 14070+0525	4980992	14h09m31.2s	+05d11m31s	0.2644
IRAS 14121-0126	25186304	14h14m45.5s	-01d40m55s	0.1502
IRAS F14242+3258	14084352	14h26m23.8s	+32d44m35s	0.1760
IRAS 14348-1447	4981248	14h37m38.2s	-15d00m24s	0.0830
IRAS F14394+5332	29040128	14h41m04.3s	+53d20m08s	0.1045
IRAS F14511+1406	4168960	14h53m31.5s	+13d53m58s	0.1390
IRAS F14554+3858	28244224	14h57m22.7s	+38d46m28s	0.0735
IRAS 15225+2350	10112512	15h24m43.9s	+23d40m10s	0.1390
IRAS 15250+3609	4983040	15h26m59.3s	+35d58m37s	0.0552
Arp 220	4983808	15h34m57.2s	+23d30m11s	0.0181
FESS J160655.82+541500.7	24189952	16h06m55.8s	+54d15m00s	0.2060
IRAS F16073+0209	17546496	16h09m49.7s	+02d01m30s	0.2230
IRAS 16090-0139	4984576	16h11m40.4s	-01d47m05s	0.1336
FESS J161759.22+541501.3	24163328	16h17m59.2s	+54d15m01s	0.1339
IRAS F16156+0146	17546752	16h18m09.3s	+01d39m22s	0.1320
IRAS F16242+2218	17547008	16h26m26.0s	+22d11m45s	0.1570
IRAS F16305+4823	22135040	16h31m58.7s	+48d17m22s	0.0874
IRAS 16300+1558	4985088	16h32m21.4s	+15d51m45s	0.2417
IRAS 16455+4553	14875136	16h46m58.9s	+45d48m22s	0.1906
IRAS 16468+5200W	10107136	16h48m01.3s	+51d55m43s	0.1500
IRAS 16468+5200E	10106880	16h48m01.6s	+51d55m44s	0.1500
NGC 6240	4985600	16h52m58.8s	+02d24m03s	0.0245
IRAS 17044+6720	10107904	17h04m28.4s	+67d16m28s	0.1349
IRAS F17028+3616	27194112	17h04m33.5s	+36d12m18s	0.0851
IRAS 17068+4027	4986112	17h08m32.1s	+40d23m28s	0.1790
IRAS 17208-0014	4986624	17h23m21.9s	-00d17m00s	0.0428
IRAS 17463+5806	4987392	17h47m04.7s	+58d05m22s	0.3090
IRAS 17540+2935	18204928	17h55m56.1s	+29d35m26s	0.1081
IRAS 18443+7433	4987904	18h42m54.7s	+74d36m21s	0.1347
IRAS 18531-4616	4988160	18h56m53.0s	-46d12m46s	0.1408
IRAS 18588+3517	18205440	19h00m41.1s	+35d21m27s	0.1067
IRAS 20087-0308	4989440	20h11m23.8s	-02d59m50s	0.1057
IRAS 20100-4156	4989696	20h13m29.8s	-41d47m34s	0.1296
IRAS 20109-3003	14875904	20h14m05.5s	-29d53m53s	0.1407
IRAS 20286+1846	18205696	20h30m54.4s	+18d56m37s	0.1358
IRAS 20551-4250	4990208	20h58m26.7s	-42d39m01s	0.0430
IRAS 21077+3358	18205952	21h09m50.6s	+34d10m34s	0.1767
IRAS 21272+2514	4990464	21h29m29.3s	+25d27m55s	0.1508
IRAS F21329-2346	10448640, 10108160	21h35m45.8s	-23d32m34s	0.1251
IRAS F21541-0800	27441408	21h56m49.5s	-07d45m32s	0.0551
NGC 7172	18513920	22h02m01.9s	-31d52m11s	0.0087
IRAS 22088-1831W	25189120	22h11m33.7s	-18d17m06s	0.1702
IRAS 22088-1831E	25189376	22h11m33.8s	-18d17m05s	0.1702
IRAS 22116+0437	18206464	22h14m10.3s	+04d52m26s	0.1938
NGC 7479 ^b	22093312	23h04m56.6s	+12d19m22s	0.0079
IRAS 23129+2548	4991488	23h15m21.4s	+26d04m32s	0.1789
IRAS F23234+0946	10449152, 10108416	23h25m56.2s	+10d02m50s	0.1279
IRAS 23230-6926	4992000	23h26m03.5s	-69d10m20s	0.1066
IRAS 23253-5415	4992256	23h28m06.1s	-53d58m30s	0.1300
IRAS 23365+3604	4992512	23h39m01.2s	+36d21m09s	0.0645

Notes. Column 1: the name of the object; Column 2: AORkey (Spitzer/IRS identification number); Columns 3, 4: the position of the object; Column 5: the redshift cited from the NASA/IPAC Extragalactic Database (NED). ^(a) The spectrum of NGC 1377 is unavailable in CASSIS. We retrieved the spectral data from the summary of the SINGS Legacy project in the NASA/IPAC IR Science Archive (IRSA). ^(b) The SL order 2 spectrum of NGC 7479 is unavailable in CASSIS. We retrieved it from the Spitzer Heritage Archive (SHA).

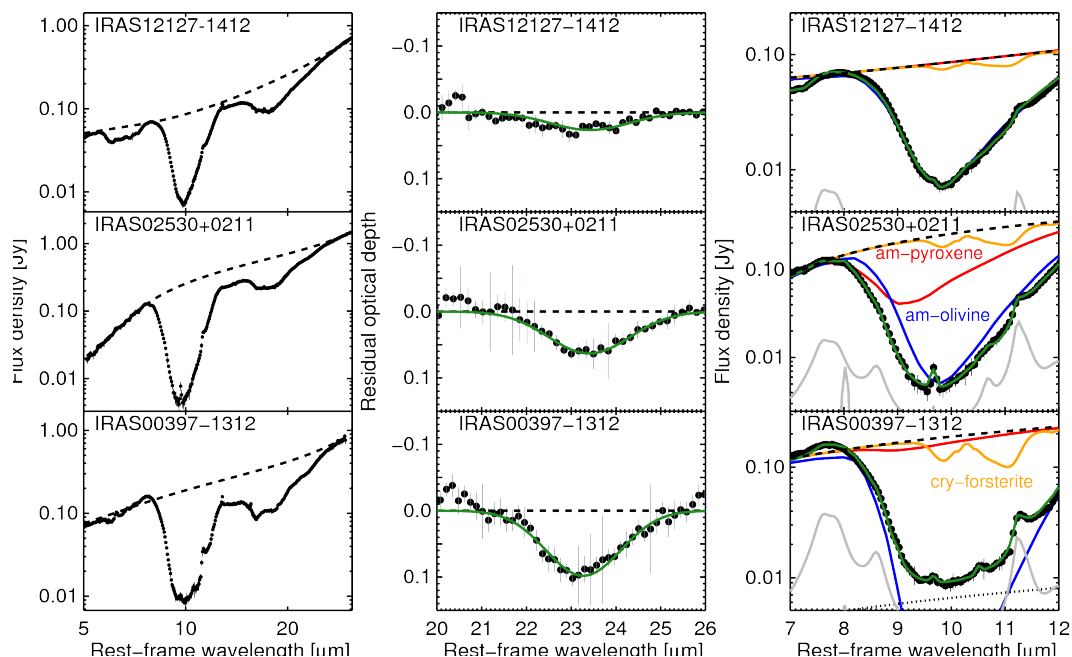


Fig. 1. Examples of the 5.3–12 μm spectral fitting. Left panels show the retrieved mid-IR spectra and the estimated absorption-free continua. Middle panels show the Gaussian fits to the 23 μm features. Results of the 5.3–12 μm spectral fitting are shown in the right panels. In the right panels, the green solid lines show the best-fit models, the absorption components of which are composed of amorphous pyroxene (red lines; $F_{\text{hot,AGN}} \exp(-\tau_{\text{pyr}})$ in equation 1), amorphous olivine (blue lines; $F_{\text{hot,AGN}} \exp(-\tau_{\text{ol}})$) and crystalline forsterite (orange lines; $F_{\text{hot,AGN}} \exp(-\tau_{\text{cry}})$). The black dashed, dotted and grey solid lines represent the absorption-free continuum ($F_{\text{hot,AGN}}$), the unobscured continuum ($F_{\text{hot,unobs}}$) and the PAH and line emission ($F_{\text{PAH}} + F_{\text{line}}$) components, respectively. Note that the unobscured continuum component falls below the plotted area for IRAS 12127–1412 and IRAS 02530+0211.

Spoon et al. (2006), while it does not match the spectra with other prominent spectral features such as those due to PAHs and ices in the wavelength range of 5–8 μm . Nardini et al. (2010) report that the 5–8 μm spectra of 164 ULIRGs, covering 68 spectra in our sample, are reproduced well using a power-law function as an absorption-free continuum. Therefore we reproduce the absorption-free continuum using a power-law function at 5.3–8 μm and a spline curve smoothly connected to the longer wavelength end of the spectrum. The spline curve is determined by using the pivot points anchored at 7.1 and 7.5 μm on the power-law continuum and 30 and 31 μm on the observed spectrum. The dashed lines in the left panel of Fig. 1 show three examples of the absorption-free continua obtained by the 5.3–12 μm spectral fitting. The sample objects whose redshifts are larger than 0.3 are not observed at the rest wavelength range longer than 30 μm , and thus the pivot points at 30 and 31 μm are extrapolated from the observed spectra assuming a power-law function.

The optical depth of the 10 μm silicate feature, τ_{sil} , is composed of three dust species using the following equation:

$$\tau_{\text{sil}} = \sum_i \tau_i = \sum_i N_i \kappa_i, \quad (2)$$

where N_i and κ_i are the mass column density and the mass absorption coefficient (MAC) of each silicate dust component, respectively. We reproduce the absorption features due to water ice at 6 μm and hydrogenated amorphous carbon (HAC) at 6.85 and 7.25 μm considering a screen geometry that the hot dust in the nuclear region is covered with colder dust clouds with water ice and HAC. For water ice and HAC opacity models, we use the template derived from the spectrum of the deeply obscured ULIRG IRAS F00183–7111 in Marshall et al. (2007) and a Gaussian function, respectively. However, the water ice template cannot well reproduce some of the spectra in our sample

well, as also pointed out in Nardini et al. (2008). For example, the spectrum of IRAS 12127–1412 shows a broader absorption feature, which extends to $\sim 7.5 \mu\text{m}$, than that of IRAS F00183–7111. The difference in the absorption feature is likely to be caused by complex compositions of processed ices including other organic species (Boogert et al. 2015). Thus we add other templates of water ice as additional absorption components derived from the spectra of IRAS 12127–1412 and NGC 4418, which show little PAH emission similar to that of IRAS F00183–7111, by spline interpolation to estimate an absorption-free continuum. For the HAC absorptions, we fix the full width at half-maxima (FWHMs) at 0.17 μm , and the central wavelengths at 6.85 and 7.25 μm . We apply the Draine & Li (2007) model to the PAH emission, F_{PAH} , assuming the typical size distribution of the diffuse ISM of star-forming galaxies. The ionization fraction of PAHs is set to be free considering different radiation fields in the circumnuclear environments, as mentioned in Kaneda et al. (2008) for elliptical galaxies. We find an emission feature at 10.68 μm stronger than those predicted by the Draine & Li (2007) model, which is suggested to originate from dehydrogenated PAHs (Mackie et al. 2015). Hence we consider an additional emission component using a Drude function, both the FWHM and central wavelength are fixed according to the resonance parameter shown in Draine & Li (2007). We also consider the interstellar extinction on the PAH emission assuming the well-mixed geometry, where we adopt the extinction curve described in Chiar & Tielens (2006). A Gaussian function is assumed for the profiles of atomic and molecular line emission components, F_{line} , both widths and central wavelengths of which are fixed at the typical parameters described in Marshall et al. (2007). Tsuchikawa et al. (2019) also suggest that the sharpness of the 10 μm silicate feature of heavily obscured AGNs is variable from galaxy to galaxy, which is likely to be attributed to the

saturation by an unobscured emission component. Therefore, we added a continuum emission component of unobscured hot dust, $F_{\text{hot,unobs}}$, using the spectral profile of $F_{\text{hot,AGN}}$ in order to explain the difference in the sharpness¹.

3.2. Dust properties

We decompose τ_{sil} to three dust components, amorphous olivine ($\text{Mg}_{2x}\text{Fe}_{2(1-x)}\text{SiO}_4$), amorphous pyroxene ($\text{Mg}_x\text{Fe}_{1-x}\text{SiO}_3$) and crystalline forsterite (Mg_2SiO_4). Amorphous olivine, the main component of the diffuse ISM in our Galaxy (Draine 2003), is reported to reproduce the $10\ \mu\text{m}$ feature of heavily obscured AGNs well (Spoon et al. 2006; Tsuchikawa et al. 2019). Crystalline forsterite is also known to compose the silicate dust in heavily obscured AGNs on the basis of detections of absorption features at 11, 16, 19 and $23\ \mu\text{m}$ (Spoon et al. 2006; Stierwalt et al. 2014). Tsuchikawa et al. (2019) report that the wings of the $10\ \mu\text{m}$ silicate absorption features shown in the spectra of the heavily obscured AGNs significantly vary from galaxy to galaxy especially on the shorter wavelength side. In other words, the central wavelengths of the $10\ \mu\text{m}$ features are variable among the heavily obscured AGNs. The difference is likely to be caused by a mineralogical composition ratio of amorphous olivine and pyroxene, since the absorption efficiencies of amorphous olivine and pyroxene have different peak wavelengths of ~ 9.8 and $\sim 9.3\ \mu\text{m}$, respectively (Dorschner et al. 1995). Accordingly, we also consider an amorphous pyroxene component in the spectral fitting.

The MACs of amorphous olivine and amorphous pyroxene, κ_{ol} and κ_{pyr} , are represented by $3Q_{\text{abs,ol}}/4a\rho_{\text{ol}}$ and $3Q_{\text{abs,pyr}}/4a\rho_{\text{pyr}}$, respectively, assuming a spherical homogeneous dust grain. The dust size, a , is fixed at $0.1\ \mu\text{m}$, and the absorption coefficients, $Q_{\text{abs,ol}}$ and $Q_{\text{abs,pyr}}$, are calculated from the optical constants of amorphous olivine (MgFeSiO_4) and amorphous pyroxene ($\text{Mg}_{0.5}\text{Fe}_{0.5}\text{SiO}_3$) obtained by the laboratory measurement of Dorschner et al. (1995) according to the Mie theory (Bohren & Huffman 1998). The mass densities of amorphous olivine and pyroxene, ρ_{ol} and ρ_{pyr} , are 3.71 and $3.20\ \text{g cm}^{-3}$, respectively (Dorschner et al. 1995). We use κ_{cry} of free-flying crystalline forsterite in aerosol measured by Tamanai et al. (2006), the peak wavelengths of which are known to be consistent with the crystalline forsterite features observed in our Galaxy (Wright et al. 2016). The measurements using the aerosol technique are not quantitative, and hence we normalize κ_{cry} measured by Tamanai et al. (2006) assuming $\kappa_{\text{cry}}(23\ \mu\text{m}) = 3.7 \times 10^3\ \text{cm}^2\text{g}^{-1}$ (Fabian et al. 2001).

The $11\ \mu\text{m}$ crystalline feature is easily affected by the PAH emission feature at $11.3\ \mu\text{m}$, and hence it is hard to derive the crystallinity robustly by decomposing the $11\ \mu\text{m}$ crystalline feature from the $10\ \mu\text{m}$ amorphous feature. On the other hand, we clearly detect the $23\ \mu\text{m}$ crystalline feature without being affected by the PAH emission, which is also pointed out in Stierwalt et al. (2014). Therefore we fix N_{cry} in the spectral fitting using the information on the $23\ \mu\text{m}$ crystalline feature, which is determined by spectral fitting of the $23\ \mu\text{m}$ feature with a Gaussian function (see the middle panel of Fig. 1). The absorption-free continuum for the $23\ \mu\text{m}$ feature is assumed using a spline curve, the pivot points of which are anchored at 20, 21, 25.5 and $30\ \mu\text{m}$. The central wavelength is restricted to the wavelength range of $23.0\text{--}23.5\ \mu\text{m}$. In addition, as seen in the 16, 19 and $23\ \mu\text{m}$ crystalline features in figure 5 of Spoon et al. (2006), the crystalline features at longer wavelengths tend to show smaller

¹ We verify the validity of the continuum emission component of unobscured hot dust in Appendix A.

apparent optical depths in the spectra of ULIRGs contrary to the laboratory measurements of κ_{cry} , which is probably caused by the radiative transfer effects or the dilution by continuum emission from cold dust. Hence we estimate N_{cry} for all the objects in our sample by calculating $CF_{108572} \times \tau_{\text{cry}}(23\ \mu\text{m})/\kappa_{\text{cry}}(11\ \mu\text{m})$, where CF_{108572} is defined as $\tau_{\text{cry},108572}(11\ \mu\text{m})/\tau_{\text{cry},108572}(23\ \mu\text{m})$ and obtained from the spectral decomposition of the $10\ \mu\text{m}$ silicate feature of IRAS 08572+3915 which shows little PAH emission.

It is difficult to obtain the uncertainty of the correction by CF_{108572} because the crystalline features at ~ 9.8 and $\sim 11.1\ \mu\text{m}$ are diluted in almost all the sample spectra. On the other hand, the crystalline feature at $\sim 16\ \mu\text{m}$ is not diluted much, and thus we investigate $\tau(16\ \mu\text{m})/\tau(23\ \mu\text{m})$, instead of $\tau(11\ \mu\text{m})/\tau(23\ \mu\text{m})$, for 12 sources shown in Spoon et al. (2006). From figure 4 in Spoon et al. (2006), the mean and standard deviation of the $\tau(16\ \mu\text{m})/\tau(23\ \mu\text{m})$ are found to be 1.71 and 0.46, respectively, and the value of $\tau(16\ \mu\text{m})/\tau(23\ \mu\text{m})$ for IRAS 08572+3915 is 1.46. We investigated the effect of the difference between 1.71 and 1.46 on the $5.3\text{--}12\ \mu\text{m}$ spectral fitting, assuming N_{cry} 1.71/1.46 times larger. As a result, the results of the fits for all the sample did not change significantly with a significance level of 5% by the F-test. Therefore we conclude that the uncertainty of the correction by CF_{108572} does not affect the results of the $5.3\text{--}12\ \mu\text{m}$ spectral fitting significantly.

3.3. Fitting procedure

We performed the spectral fitting in the following four steps, in which we use the Levenberg–Marquardt algorithm (Levenberg 1944; Marquardt 1963) for the χ^2 minimization: (1) we determined the amplitudes of line emissions by spectral fitting for a narrow wavelength range assuming a quadratic function as a local continuum, and then fixed those parameters in the subsequent procedure. (2) We tentatively fitted the spectrum of the wavelength range of $5.3\text{--}7.8\ \mu\text{m}$ to obtain initial parameters for the following fitting processes. As for the fitting function, we assume equation 1 setting τ_{sil} and $F_{\text{hot,unobs}}$ to be zero as the silicate feature is out of the wavelength range. Using the initial parameters thus obtained, we fitted the spectrum of the wavelength range of $5.3\text{--}12\ \mu\text{m}$. (3) We obtained CF_{108572} (defined in the previous subsection) by fitting the $5.3\text{--}12\ \mu\text{m}$ spectrum of IRAS 08572+3915 with equation 1 where free parameters are the mass column density of crystalline forsterite, N_{cry} , as well as the parameters in Table 2. (4) We derived the properties of dust through the $5.3\text{--}12\ \mu\text{m}$ spectral fitting to all the sample spectra. The free parameters are the same as in step (3) except that N_{cry} is fixed at $CF_{108572} \times \tau_{\text{cry}}(23\ \mu\text{m})/\kappa_{\text{cry}}(11\ \mu\text{m})$.

The right panel of Fig. 1 shows examples of the results of the spectral decomposition (see Appendix B for all the sample galaxies). Although 20% of the fits to the spectra, which have high signal-to-noise ratio, are not acceptable on the basis of the χ^2 statistics with a significance level of 0.05, which is possibly caused mainly by neglecting the uncertainties of the absorption efficiency and the PAH model, the model is overall fitted to the spectra in our sample well enough to characterize the mineralogical composition and crystallinity. The uncertainties of the fitting parameters are obtained by the Monte Carlo method of fitting 100 spectra with Gaussian noises.

We consider whether a good fit can be achieved with significantly different sets of parameters in terms of parameter degeneracies. The spectral profile of the silicate absorption feature is determined by the mass ratio of amorphous olivine to pyroxene, $f_{\text{ol/pyr}} = N_{\text{ol}}/N_{\text{pyr}}$, and the ratio of the unobscured to absorption-

Table 2. Free parameters in the 5.3–12 μm spectral fitting to all the sample spectra.

Component	Parameter	Description
$F_{\text{hot,AGN}}$	$A_{\text{hot,AGN}}$	Amplitude of the 5.3–8 μm hot dust continuum emission
	$\Gamma_{\text{hot,AGN}}$	Power-law index of the 5.3–8 μm hot dust continuum emission
τ_{sil}	N_{ol}	Mass column density of amorphous olivine
	N_{pyr}	Mass column density of amorphous pyroxene
$\tau_{\text{ice+HAC}}$	$\tau_{\text{ice,I00183}}$	Amplitude of the H ₂ O ice absorption template (IRAS F00183–7111)
	$\tau_{\text{ice,I12127}}$	Amplitude of the H ₂ O ice absorption template (IRAS 12127–1412)
	$\tau_{\text{ice,N4418}}$	Amplitude of the H ₂ O ice absorption template (NGC 4418)
	$\tau_{\text{HAC,6.85}\mu\text{m}}$	Amplitude of the HAC absorption at 6.85 μm
F_{PAH}	$\tau_{\text{HAC,7.25}\mu\text{m}}$	Amplitude of the HAC absorption at 7.25 μm
	A_{PAH}	Amplitude of the PAH emission
	x_{ion}	Ionization fraction of PAHs
	$A_{\text{PAH,10.68}}$	Amplitude of the 10.68 μm PAH emission
	τ_{PAH}	Amplitude of the optical depth of the PAH emission
$F_{\text{hot,unobs}}$	$A_{\text{hot,unobs}}$	Amplitude of the unobscured hot dust continuum

free continua, $f_{\text{unobs}} = A_{\text{hot,unobs}}/A_{\text{hot,AGN}}$. We investigate the $\Delta\chi^2$ distribution within the parameter ranges of $f_{\text{ol/pyr}} = [0, \infty]$ and $f_{\text{unobs}} = [0, 1]$. In this analysis, free parameters are the total mass column density of silicate dust and the normalization of the continuum emission, while we fix the parameters of the power-law index of the continuum emission, the mass column density of crystalline forsterite, the amplitudes of the ice and HAC absorption templates, all the parameters associated with the PAH emission since they are determined almost uniquely based on the information outside the wavelength range of 8–12 μm and on the narrow PAH emission feature at 11.3 μm . From the $\Delta\chi^2$ distribution thus obtained, we confirm that the different sets of the parameters do not produce a significant fit in the spectral fitting for all the sample spectra.

4. Results

In Fig. 2, we show the histograms of the mass column densities of amorphous olivine, N_{ol} , amorphous pyroxene, N_{pyr} , and crystalline forsterite, N_{cry} , obtained by the spectral fitting. We summarize the median values and the 25th and 75th percentiles in Table 3 (see Appendix B for all the sample galaxies). The histogram of N_{ol} in our sample shows a relatively symmetric distribution centered around $1.7 \times 10^{-3} \text{ g cm}^{-2}$, which corresponds to the peak optical depth of 5.5 for the 10 μm feature. On the other hand, the histograms of N_{pyr} and N_{cry} show asymmetric distributions with tails at larger column densities. Furthermore, we find that the sample galaxies have N_{ol} more than one order of magnitude higher than N_{pyr} and N_{cry} on average, and hence amorphous olivine is likely to be the main component of the silicate dust obscuring AGNs.

We derive the abundances of the minor components by calculating the mass fractions, $N_{\text{pyr}}/N_{\text{all}}$ and $N_{\text{cry}}/N_{\text{all}}$, where $N_{\text{all}} = N_{\text{ol}} + N_{\text{pyr}} + N_{\text{cry}}$. In Fig. 3, we show the histograms of the resultant $N_{\text{pyr}}/N_{\text{all}}$ and $N_{\text{cry}}/N_{\text{all}}$, the median fractions and the 25th and 75th percentiles of which are also summarized in Table 3. We find that more than half of our sample have $N_{\text{pyr}}/N_{\text{all}} < 5\%$, while 10% of our sample have relatively high values $N_{\text{pyr}}/N_{\text{all}} > 15\%$. The histogram of $N_{\text{cry}}/N_{\text{all}}$ shows a relatively uniform distribution from 0 to 13%. Figure 3 also shows the presence of significant relationship between $N_{\text{cry}}/N_{\text{all}}$ and $N_{\text{pyr}}/N_{\text{all}}$, which indicates that the mass fractions of the minor components positively correlate to each other. On the other hand, $N_{\text{pyr}}/N_{\text{all}}$ and $N_{\text{cry}}/N_{\text{all}}$ do not correlate to the equivalent width of the PAH fea-

ture at 6.2 μm and the total optical depth of silicates with a significance level of 0.01.

5. Discussion

5.1. Properties of silicate dust in heavily obscured AGNs compared with those in our Galaxy

The mineralogical composition in our Galaxy is observationally known to be variable depending on the environments where silicate dust exists. Demyk et al. (2001) suggest the evolution of amorphous silicate from amorphous olivine newly formed around evolved stars to amorphous pyroxene around young stars. Indeed, the 10 μm features of newly formed dust observed around evolved stars are fitted well with amorphous silicate with olivine-type stoichiometry (e.g., Demyk et al. 2000; Do-Duy et al. 2020), while a typical spectrum of the diffuse ISM requires a small mass fraction of amorphous pyroxene (olivine:pyroxene = 85:15 for the Sgr A* spectrum; Kemper et al. 2004). Furthermore, it is suggested that the pyroxene mass fractions in molecular clouds and circumstellar regions of young stellar objects (YSOs) are higher than those of the diffuse ISM dust (e.g., Demyk et al. 1999; Van Breemen et al. 2011; Do-Duy et al. 2020). Amorphous pyroxene is reported to be transformed from crystalline forsterite by ion irradiation (Demyk et al. 2001; Rietmeijer 2009), and thus the ion bombardments can explain the evolution of amorphous silicate. Pyroxene-type equilibrated dust is also formed from the ISM dust by vaporization and recondensation in dense and hot environments of circumstellar disks of YSOs (Gail 2004). We show the pyroxene mass fraction of silicate dust toward Sgr A* as a red vertical dotted line in the histogram of Fig. 3, indicating an overall lower mass fraction of the amorphous pyroxene in the heavily obscured AGNs than that in the typical diffuse ISM in our Galaxy. Accordingly, the silicate dust obscuring AGNs is likely to consist of newly formed dust originated from circumnuclear starburst activities.

In general, the crystallinity is known to be high in winds from evolved stars (10–15%; e.g., Kemper et al. 2001; Molster et al. 2002) and circumstellar regions surrounding YSOs ($\sim 15\%$; e.g., van Boekel et al. 2005; Sargent et al. 2009). On the other hand, crystalline silicate dust is almost absent in the diffuse ISM and molecular clouds ($\sim 1\text{--}2\%$; e.g., Kemper et al. 2004; Van Breemen et al. 2011; Do-Duy et al. 2020), and hence it is suggested that amorphization by the ion bombardments is important (e.g., Demyk et al. 2001; Kemper et al. 2004). The high

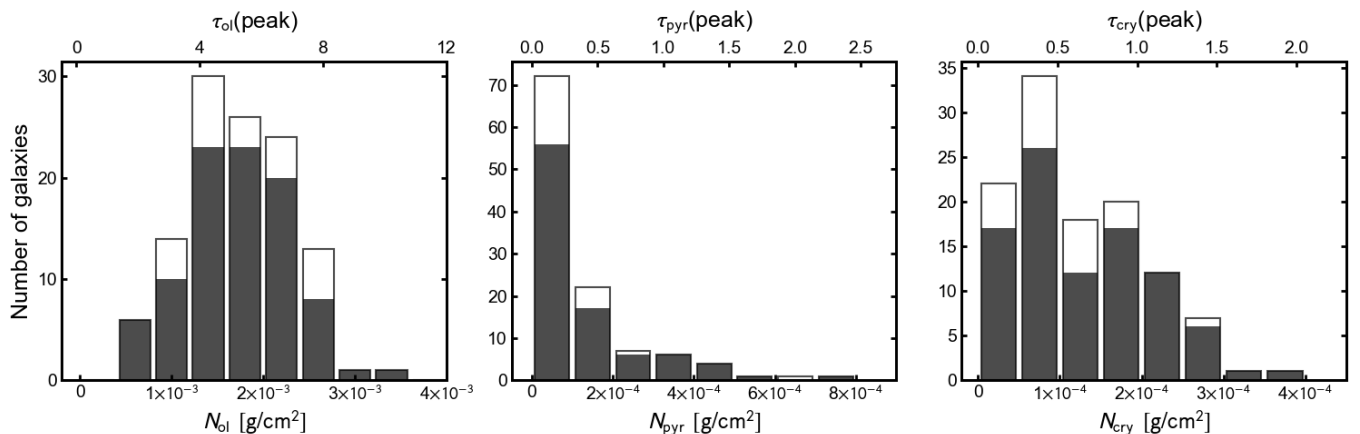


Fig. 2. Histograms of the mass column densities of amorphous olivine (N_{ol} ; *left*), amorphous pyroxene (N_{pyr} ; *center*) and crystalline forsterite (N_{cry} ; *right*). The optical depths at the peak wavelengths corresponding to the mass column densities are shown in the upper x-axes. The peak wavelengths used for calculating the optical depths of amorphous olivine, amorphous pyroxene and crystalline forsterite are 9.8, 9.2 and 11.0 μm , respectively. Black and white bars indicate the sources whose 5.3–12 μm spectral fits are accepted and those rejected, respectively, on the basis of the χ^2 statistics with a significance level of 0.05.

Table 3. General properties of the silicate dust in our sample AGNs

	N_{ol} [g/cm^2]	$\tau_{ol}(\text{peak})$	N_{pyr} [g/cm^2]	$\tau_{pyr}(\text{peak})$	N_{cry} [g/cm^2]	$\tau_{cry}(\text{peak})$	N_{pyr}/N_{all} [%]	N_{cry}/N_{all} [%]
Median ^a	1.7×10^{-3}	5.5	5.0×10^{-5}	0.20	1.0×10^{-4}	0.38	2.2	6.2
25th ^b	1.4×10^{-3}	4.2	0	0	5.9×10^{-5}	0.22	0	3.3
75th ^c	2.2×10^{-3}	6.9	1.6×10^{-4}	0.67	1.8×10^{-4}	0.66	7.9	8.9

Notes. ^(a) The median values. ^(b) The 25th percentiles. ^(c) The 75th percentiles.

crystallinity of the silicate dust surrounding YSOs is considered to be caused by thermal annealing in the hot environment close to the central star (e.g., van Boekel et al. 2005; Sargent et al. 2009). The average crystallinity of $\sim 6\%$ in the heavily obscured AGNs in Table 3 and Fig. 3 is closer to those of newly formed dust around the evolved stars rather than the diffuse ISM dust in our Galaxy. It is possible that the overall high crystallinity of the silicate dust obscuring AGNs originates from evolved massive stars in the starburst environments, as also mentioned in Spoon et al. (2006). The crystallinity is determined by the balance of dust production, amorphization and destruction rates. Kemper et al. (2011) simulate whether the starburst activities alone can explain the crystallinities of 6.5–13% suggested in Spoon et al. (2006), and show that such a high crystallinity cannot be explained unless extreme input parameters are assumed for such as the star formation rate and the initial crystallinity in the stellar ejecta. If a top heavy initial mass function (IMF) (Zhang et al. 2018) is assumed instead of the IMF in e.g., Kroupa (2001), high crystallinity may be achieved temporarily because the starburst activity produces large amounts of dust on a shorter timescale than that for amorphization. We do not consider this possibility in the following discussion. Accordingly, in order to explain the overall trend of high crystallinity, we consider re-crystallization of amorphous silicate or production of crystalline silicate other than starburst activities.

Although crystallization occurs in high-temperature environments at ~ 1000 K, the crystalline silicate in heavily obscured AGNs is considered to be located in relatively outer cooler regions because we detect the crystalline features only in the absorption at the wavelength of 23 μm . For a re-crystallization mechanism of amorphous silicate in cooler regions in heavily obscured AGNs, we consider a possibility of a localized crys-

tallization due to a transient heating by shock waves (Harker & Desch 2002), driven by supernovae in the circumnuclear starburst and/or outflow if the shocks can anneal silicate dust up to ~ 1000 K. Because the chemical equilibrium cannot be achieved by a short annealing time typical of the shock heating, crystalline enstatite, the Mg end member of pyroxene, is unlikely to be formed (Gail 2004), which is consistent with the spectral characteristics of our sample spectra. Ions accelerated in shock wave propagation and cosmic rays, which are considered to be accelerated in the shock front (e.g., Bell 1978), can destroy the crystalline structure of silicate dust (Demyk et al. 2001), which negatively acts for the enrichment of the crystalline silicate. Therefore we consider that the localized crystallization due to a transient heating by shock waves is hard to cause the high crystallinity.

Another possibility is that the crystalline silicate is produced or processed in the high temperature environments close to the nucleus and transported to outer cooler region by radial mixing or outflow. Indeed, Markwick-Kemper et al. (2007) report the emission feature due to crystalline forsterite in a quasar wind spectrum. However, Spoon et al. (2006) conclude that this possibility is unlikely because of the following two reasons: one is that crystalline feature is not detected in the central 2 pc of NGC 1068 in the mid-IR interferometric observation in Jaffe et al. (2004). Raban et al. (2009) report the follow-up observation of NGC 1068 with a different position angle and longer baseline length than those in Jaffe et al. (2004). We find that the 11 μm crystalline feature is significantly detected in the mid-IR spectra shown in Raban et al. (2009) although Raban et al. (2009) do not mention the crystalline feature. Hence the crystallinity of the central region of NGC1068 rather supports the picture that crystalline silicate originates from AGNs. The other reason is that

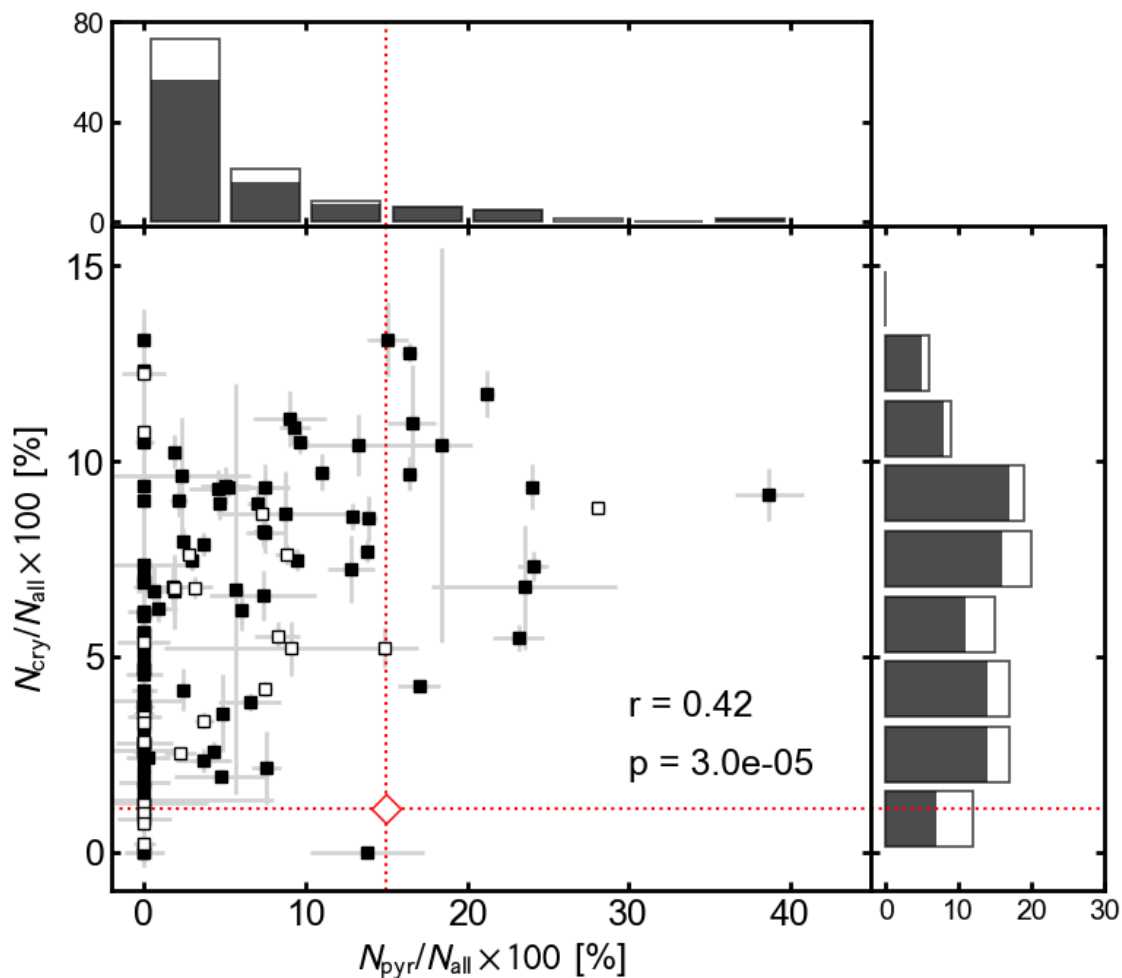


Fig. 3. Correlation plot between $N_{\text{cry}}/N_{\text{all}}$ and $N_{\text{pyr}}/N_{\text{all}}$ and their histograms. Filled and open black squares show the objects whose 5.3–12 μm spectral fits are accepted and those rejected on the basis of the χ^2 statistics with a significance level of 0.05, respectively. Black and white bars in the histograms also indicate the sources in which the spectral fits are accepted and rejected, respectively. The correlation coefficient and the p-value for the accepted sample are shown at the bottom right corner of the correlation plot. Red diamond and dotted lines show the silicate dust properties obtained from the Sgr A* spectrum, a typical spectrum of the diffuse ISM in our Galaxy (Kemper et al. 2004).

we have to newly introduce a large-scale transportation mechanism itself. Recent dynamical views of an AGN torus (e.g., Wada 2012) are likely to explain a large-scale transportation. Indeed, molecular outflows have been observed in nearby obscured AGNs including a lot of objects in our sample in the recent years (e.g., Aalto et al. 2012; Veilleux et al. 2013; Lutz et al. 2020). For example, NGC 1377 in our sample is known to have a 150 pc-scale molecular outflow. The large mass outflow rate suggests the presence of a feedback loop of cyclic outflow (e.g., Aalto et al. 2020). The projected size of the 800 μm nuclear dust continuum of NGC 1377 is observed to be ~ 4 pc (Aalto et al. 2020). The timescale for amorphization due to the cosmic-ray bombardment is estimated to be 70 Myr (Bringa et al. 2007). Thus the dust radial velocity needs to be faster than 0.05 km/s, which is considerably slower as compared to the outflow velocity of the molecular wind, 90 km/s, measured by Aalto et al. (2020). Kozasa & Sogawa (1999) report that it takes only 30 days processing into crystalline forsterite at the dust temperature of 1000 K, which is negligibly short. Thus it is possible that crystalline silicate processed around the nucleus is transported to outer regions by the feedback loop of outflow.

5.2. Origin of the difference in the silicate dust properties

In Fig. 3, we find the positive correlation between $N_{\text{cry}}/N_{\text{all}}$ and $N_{\text{pyr}}/N_{\text{all}}$, indicating that heavily obscured AGNs with a relatively higher mass fraction of the amorphous pyroxene, which deviate from the overall trend, show a higher mass fraction of the crystalline forsterite. According to the above discussion, the amorphous olivine, the main component of silicate obscuring AGNs, is crystallized by the thermal annealing close to the nucleus and transported to the outer region. The mass fraction of the crystalline forsterite is likely to vary depending on the degree of the thermal processing or the radial transportation of silicate dust among the heavily obscured AGNs. Therefore heavily obscured AGNs with high mass fractions of the crystalline forsterite is naturally of high mass fractions of amorphous pyroxene considering that crystalline forsterite is partially transformed to amorphous pyroxene by ion bombardments in/after the radial transportation to the outer cooler region as the main formation mechanism of amorphous pyroxene. For another formation mechanism, we consider that crystalline enstatite, which is likely to be formed from the ISM dust by vaporization and recondensation (Gail 2004) in the dense and hot nuclear environment, is processed to amorphous pyroxene by cosmic-ray bom-

bardments. However, the spectral features of crystalline enstatite are not detected in the spectra of our sample, and therefore we excluded this possibility. We also find that 5 out of 15 sources with a mass fraction of $>10\%$ crystalline forsterite, which do not have a significant fraction of amorphous pyroxene, deviate from the trend of the positive correlation. Since the timescale for amorphization is considerably longer than that for the dust radial transportation as discussed in Sect. 5.1, crystalline forsterite is likely to amorphize mainly after the transportation. Hence, if we observe the sources just after the radial transportation started, the mass fraction of crystalline forsterite is likely to be high without producing a significant fraction of amorphous pyroxene. Accordingly, the difference in the silicate dust properties among the heavily obscured AGNs originates mainly from the difference in the degree of the AGN activities, that is, the thermal processing or the radial transportation.

We focus on the temperature of the circumnuclear region to confirm that the difference in $N_{\text{cry}}/N_{\text{all}}$ and $N_{\text{pyr}}/N_{\text{all}}$ originates mainly from the difference in the degree of the thermal processing. In general, H_2O ice, the sublimation temperature of which is 90 K (Tielens 2005), is assumed to exist in the mantle of dust in dense cold molecular clouds. Hence, for heavily obscured AGNs with deep ice absorptions at 3.0 and 6.0 μm , silicate dust in dense cold circumnuclear regions is likely to dominate the total silicate absorption along the line of sight. Icy dust is expected to exist in the relatively warm environment since the CO_2 ice absorption feature at 15.0 μm , the sublimation temperature of which is 50 K (Tielens 2005), are not detected for most of the ULIRGs by Lahuis et al. (2007) in contrast to the detection of the 6 μm H_2O ice feature. In our Galaxy, deep CO_2 ice absorption features are observed in dense molecular clouds (Gibb et al. 2000), and thus we conclude that dense molecular clouds in the host galaxies do not contribute to the total column density of H_2O ice. We calculate the ratio of the 6 μm optical depth of H_2O ice to the total mass column density of silicate dust, $\tau_{\text{ice}}(6 \mu\text{m})/N_{\text{all}}$, which is likely to depend on the average temperature of obscuring dust. In Fig. 4, we compare the silicate properties shown in Fig. 3 with $\tau_{\text{ice}}(6 \mu\text{m})/N_{\text{all}}$, which indicates that the obscuring silicate dust in galaxies with high $\tau_{\text{ice}}(6 \mu\text{m})/N_{\text{all}}$ tends to be of low mass fractions of amorphous pyroxene and crystalline forsterite. Hence silicate dust obscuring AGNs with a high $\tau_{\text{ice}}(6 \mu\text{m})/N_{\text{all}}$, which has a relatively low temperature, is considered to be processed less heavily. Assuming the nucleus as the heating source, cooler dust is located more distant from the nucleus, and therefore is harder to be transported from the nucleus. This is consistent with the above discussion, and thus dust processing is likely to originate from the AGN activity.

6. Conclusions

We investigate AGN activities obscured by large amounts of dust through a systematic study of silicate dust properties. We select 115 mid-IR spectra of the heavily obscured AGNs observed by Spitzer/IRS, and characterize the silicate features by spectral fitting focusing on the mineralogical composition and crystallinity. As a result, we fit the spectra well using three dust components of amorphous olivine, amorphous pyroxene and crystalline forsterite. We find that the main component of silicate dust obscuring AGNs is amorphous olivine, the average mass column density of which is one order of magnitude higher than those of amorphous pyroxene and crystalline forsterite. We also find that the mass fractions of amorphous pyroxene and crystalline forsterite significantly correlate to each other.

The overall dust properties of heavily obscured AGNs tend to be of a lower mass fraction of the amorphous pyroxene and of a higher mass fraction of the crystalline forsterite than those of the diffuse ISM in our Galaxy. The overall trend of the low mass fraction of the amorphous pyroxene suggests that silicate dust newly formed in starburst activities is abundant for the obscuring silicate dust. The overall trend of high crystallinity and the fact that crystalline features are seen only in the absorption suggest that amorphous silicate is thermally processed close to the nucleus and radially transported to an outer cooler region. Considering that amorphous pyroxene can be transformed from crystalline forsterite by ion bombardments, we can explain the positive correlation between the amorphous pyroxene and crystalline forsterite mass fractions. Therefore the difference in the dust properties among the heavily obscured AGNs originates mainly from the difference in the degree of the thermal processing or the radial transportation. We also find that heavily obscured AGNs with high ratios of the H_2O ice absorption to silicate mass column density tend to have silicate dust with lower mass fractions of amorphous pyroxene and crystalline forsterite, which is consistent with the scenario of the thermal dust processing close to the nucleus.

Acknowledgements. This work is based on observations with the Spitzer Space Telescope, which is operated by the Jet Propulsion Laboratory, California Institute of Technology under a contract with NASA, using the the Combined Atlas of Sources with Spitzer IRS Spectra (CASSIS). CASSIS is a product of the IRS instrument team, supported by NASA and JPL.

References

- Aalto, S., Falstad, N., Muller, S., et al. 2020, A&A, 640, A104
Aalto, S., Muller, S., Sakamoto, K., et al. 2012, A&A, 546, A68
Antonucci, R. 1993, ARA&A, 31, 473
Bell, A. R. 1978, MNRAS, 182, 147
Bohren, C. F. & Huffman, D. R. 1998, Absorption and Scattering of Light by Small Particles
Boogert, A. C. A., Gerakines, P. A., & Whittet, D. C. B. 2015, ARA&A, 53, 541
Bringa, E. M., Kucheyev, S. O., Loeffler, M. J., et al. 2007, ApJ, 662, 372
Chiar, J. E. & Tielens, A. G. G. M. 2006, ApJ, 637, 774
Demyk, K., Carrez, P., Leroux, H., et al. 2001, A&A, 368, L38
Demyk, K., Dartois, E., Wiesemeyer, H., Jones, A. P., & d'Hendecourt, L. 2000, A&A, 364, 170
Demyk, K., Jones, A. P., Dartois, E., Cox, P., & D'Hendecourt, L. 1999, A&A, 349, 267
Do-Duy, T., Wright, C. M., Fujiyoshi, T., et al. 2020, MNRAS, 493, 4463
Dorschner, J., Begemann, B., Henning, T., Jaeger, C., & Mutschke, H. 1995, A&A, 300, 503
Draine, B. T. 2003, ARA&A, 41, 241
Draine, B. T. & Li, A. 2007, ApJ, 657, 810
Duy, T. D. & Lawson, W. A. 2019, MNRAS, 488, L75
Fabian, D., Henning, T., Jäger, C., et al. 2001, A&A, 378, 228
Gail, H. P. 2004, A&A, 413, 571
Gibb, E. L., Whittet, D. C. B., Schutte, W. A., et al. 2000, ApJ, 536, 347
Hao, L., Weedman, D. W., Spoon, H. W. W., et al. 2007, ApJ, 655, L77
Harker, D. E. & Desch, S. J. 2002, ApJ, 565, L109
Hatziminaoglou, E., Hernán-Caballero, A., Feltre, A., & Piñol Ferrer, N. 2015, ApJ, 803, 110
Henning, T. 2010, ARA&A, 48, 21
Hopkins, P. F., Hernquist, L., Cox, T. J., & Kereš, D. 2008, ApJS, 175, 356
Houck, J. R., Roellig, T. L., van Cleve, J., et al. 2004, ApJS, 154, 18
Imanishi, M. & Dudley, C. C. 2000, ApJ, 545, 701
Imanishi, M., Dudley, C. C., Maiolino, R., et al. 2007, ApJS, 171, 72
Imanishi, M., Dudley, C. C., & Maloney, P. R. 2006, ApJ, 637, 114
Jaffe, W., Meisenheimer, K., Röttgering, H. J. A., et al. 2004, Nature, 429, 47
Kaneda, H., Onaka, T., Sakon, I., et al. 2008, ApJ, 684, 270
Kemper, F., Markwick, A. J., & Woods, P. M. 2011, MNRAS, 413, 1192
Kemper, F., Vriend, W. J., & Tielens, A. G. G. M. 2004, ApJ, 609, 826
Kemper, F., Waters, L. B. F. M., de Koter, A., & Tielens, A. G. G. M. 2001, A&A, 369, 132
Kozasa, T. & Sogawa, H. 1999, in Asymptotic Giant Branch Stars, ed. T. Le Bertre, A. Lebre, & C. Waelkens, Vol. 191, 239
Kroupa, P. 2001, MNRAS, 322, 231

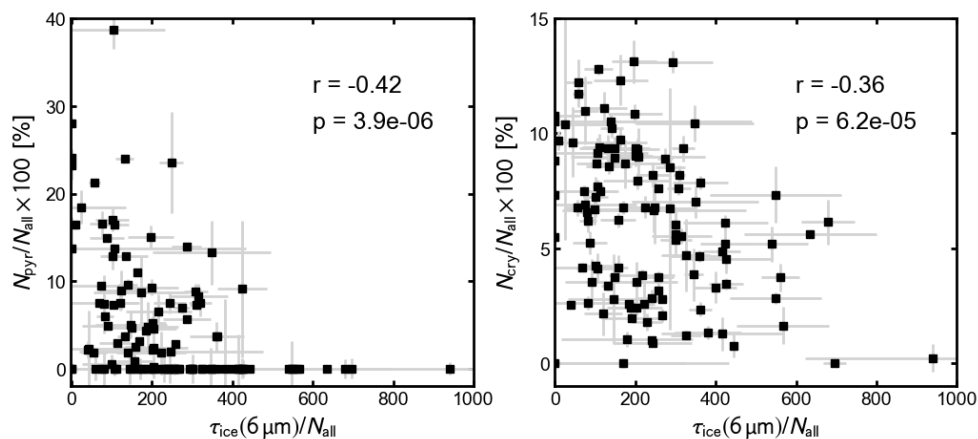


Fig. 4. Anti-correlations of $\tau_{\text{ice}}(6 \mu\text{m})/N_{\text{all}}$ with $N_{\text{cry}}/N_{\text{all}}$ (*left*) and $N_{\text{pyr}}/N_{\text{all}}$ (*right*). The correlation coefficients and the p-values for the sample are shown at the top right corners.

- Lahuis, F., Spoon, H. W. W., Tielens, A. G. G. M., et al. 2007, *ApJ*, 659, 296
 Lebouteiller, V., Barry, D. J., Goes, C., et al. 2015, *ApJS*, 218, 21
 Lebouteiller, V., Barry, D. J., Spoon, H. W. W., et al. 2011, *ApJS*, 196, 8
 Levenberg, K. 1944, *Quarterly of applied mathematics*, 2, 164
 Li, M. P., Shi, Q. J., & Li, A. 2008, *MNRAS*, 391, L49
 Lutz, D., Sturm, E., Janssen, A., et al. 2020, *A&A*, 633, A134
 Mackie, C. J., Peeters, E., Bauschlicher, C. W., J., & Cami, J. 2015, *ApJ*, 799, 131
 Markwick-Kemper, F., Gallagher, S. C., Hines, D. C., & Bouwman, J. 2007, *ApJ*, 668, L107
 Marquardt, D. W. 1963, *Journal of the society for Industrial and Applied Mathematics*, 11, 431
 Marshall, J. A., Elitzur, M., Armus, L., Diaz-Santos, T., & Charmandaris, V. 2018, *ApJ*, 858, 59
 Marshall, J. A., Herter, T. L., Armus, L., et al. 2007, *ApJ*, 670, 129
 Mathis, J. S., Rumpl, W., & Nordsieck, K. H. 1977, *ApJ*, 217, 425
 Molster, F. J., Waters, L. B. F. M., & Tielens, A. G. G. M. 2002, *A&A*, 382, 222
 Nardini, E., Risaliti, G., Salvati, M., et al. 2008, *MNRAS*, 385, L130
 Nardini, E., Risaliti, G., Watabe, Y., Salvati, M., & Sani, E. 2010, *MNRAS*, 405, 2505
 Olofsson, J., Augereau, J. C., van Dishoeck, E. F., et al. 2009, *A&A*, 507, 327
 Raban, D., Jaffe, W., Röttgering, H., Meisenheimer, K., & Tristram, K. R. W. 2009, *MNRAS*, 394, 1325
 Rietmeijer, F. J. M. 2009, *ApJ*, 705, 791
 Risaliti, G., Gilli, R., Maiolino, R., & Salvati, M. 2000, *A&A*, 357, 13
 Sargent, B. A., Forrest, W. J., Tayrien, C., et al. 2009, *ApJS*, 182, 477
 Smith, H. A., Li, A., Li, M. P., et al. 2010, *ApJ*, 716, 490
 Spoon, H. W. W., Marshall, J. A., Houck, J. R., et al. 2007, *ApJ*, 654, L49
 Spoon, H. W. W., Tielens, A. G. G. M., Armus, L., et al. 2006, *ApJ*, 638, 759
 Srinivasan, S., Kemper, F., Zhou, Y., et al. 2017, *Planet. Space Sci.*, 149, 56
 Stierwalt, S., Armus, L., Charmandaris, V., et al. 2014, *ApJ*, 790, 124
 Stierwalt, S., Armus, L., Surace, J. A., et al. 2013, *ApJS*, 206, 1
 Tamanai, A., Mutschke, H., Blum, J., & Meeus, G. 2006, *ApJ*, 648, L147
 Tielens, A. G. G. M. 2005, *The Physics and Chemistry of the Interstellar Medium*
 Tsuchikawa, T., Kaneda, H., Oyabu, S., et al. 2019, *A&A*, 626, A130
 Urry, C. M. & Padovani, P. 1995, *PASP*, 107, 803
 van Boekel, R., Min, M., Waters, L. B. F. M., et al. 2005, *A&A*, 437, 189
 Van Breemen, J. M., Min, M., Chiar, J. E., et al. 2011, *A&A*, 526, A152
 Veilleux, S., Meléndez, M., Sturm, E., et al. 2013, *ApJ*, 776, 27
 Wada, K. 2012, *ApJ*, 758, 66
 Weedman, D. W., Hao, L., Higdon, S. J. U., et al. 2005, *ApJ*, 633, 706
 Werner, M. W., Roellig, T. L., Low, F. J., et al. 2004, *ApJS*, 154, 1
 Wright, C. M., Do Duy, T., & Lawson, W. 2016, *MNRAS*, 457, 1593
 Xie, Y., Li, A., & Hao, L. 2017, *ApJS*, 228, 6
 Zhang, Z.-Y., Romano, D., Ivison, R. J., Papadopoulos, P. P., & Matteucci, F. 2018, *Nature*, 558, 260

Appendix A: Sharpness of the 10 μm silicate feature

We consider a possibility that dust properties explain the difference in the sharpness of the 10 μm silicate feature instead of that of the saturation due to the unobscured emission component. Broad 10 μm emission features seen in the spectra of type-1 AGNs are explained by larger-size or higher-porosity dust than typical 0.1 μm -sized homogeneous dust (e.g., Xie et al. 2017; Li et al. 2008), while those seen in the spectra of circumstellar disks are explained by, for instance, the combination of silica (SiO_2) at 8.6 μm , crystalline enstatite (MgSiO_3), forsterite and amorphous features (e.g., van Boekel et al. 2005; Olofsson et al. 2009). In order to identify the causes of the difference in the sharpness, we calculate the two apparent optical depth ratios $\tau_{\text{sil}}^{\text{ap}}(9 \mu\text{m})/\tau_{\text{sil}}^{\text{ap}}(10 \mu\text{m})$ and $\tau_{\text{sil}}^{\text{ap}}(12 \mu\text{m})/\tau_{\text{sil}}^{\text{ap}}(10 \mu\text{m})$ using the optical depths $\tau_{\text{sil}}^{\text{ap}}(\lambda)$ determined by the absorption-free continuum of $F_{\text{hot,AGN}}$. Both smaller $\tau_{\text{sil}}^{\text{ap}}(9 \mu\text{m})/\tau_{\text{sil}}^{\text{ap}}(10 \mu\text{m})$ and $\tau_{\text{sil}}^{\text{ap}}(12 \mu\text{m})/\tau_{\text{sil}}^{\text{ap}}(10 \mu\text{m})$ indicate sharper 10 μm feature if the central wavelength of the feature is at around 10 μm . Figure A.1 shows the relationship between $\tau_{\text{sil}}^{\text{ap}}(12 \mu\text{m})/\tau_{\text{sil}}^{\text{ap}}(10 \mu\text{m})$ and $\tau_{\text{sil}}^{\text{ap}}(9 \mu\text{m})/\tau_{\text{sil}}^{\text{ap}}(10 \mu\text{m})$, which clearly shows a tight positive correlation. If the size or porosity of dust caused the difference in the sharpness, a negative correlation between the ratios should be observed because the central wavelength of the 10 μm feature shifts towards longer wavelengths due to larger-sized or higher-porosity amorphous silicate. Therefore it is unlikely that the difference in the sharpness is caused by the size or porosity of dust.

We simulate the saturation effects due to the unobscured hot dust emission using the absorption efficiency of amorphous olivine, $Q_{\text{abs,ol}}$, which is the main component of the silicate dust in our sample, by changing the contribution levels of the unobscured component. We assume the mass column density of the silicate dust of $1.7 \times 10^{-3} \text{ g/cm}^2$, the mean mass column density of amorphous olivine in our sample obtained by the spectral fitting, for the simulation. The relationship between $\tau_{\text{sil}}^{\text{ap}}(12 \mu\text{m})/\tau_{\text{sil}}^{\text{ap}}(10 \mu\text{m})$ and $\tau_{\text{sil}}^{\text{ap}}(9 \mu\text{m})/\tau_{\text{sil}}^{\text{ap}}(10 \mu\text{m})$ (the dashed line in Fig. A.1) traces the trend of the data points well, although there is a slight offset presumably due to the presence of PAH or line features. Figure A.1 is color-coded according to the mass column density of silicate dust, N_{all} obtained by the 5.3–12 μm spectral fitting. We find that the spectra with deeper absorptions show flatter profiles at the bottom of the feature. When the saturation causes the difference in the sharpness, the trend is reasonable considering that the ratio of the unobscured hot dust emission to absorption-free continuum emission does not change much. Therefore we conclude that the unobscured emission component is likely to cause the difference in the sharpness.

In the 5.3–12 μm spectral fitting, we assume the spectral profile of the absorption-free continuum emission due to the hot dust heated by AGN, not the extended star-formation component responsible for the PAH emission. We verify the validity of this assumption. We investigate the relationship between the equivalent width of the PAH feature at 6.2 μm and the ratio of $A_{\text{hot,unobs}}$ to $A_{\text{hot,AGN}}$, which is expected to correlate positively if the weak continuum filling in the 9.7 μm feature is attributed to the extended star-formation component. The correlation coefficient and the p-value are 0.08 and 0.37, respectively, which do not indicate a significant correlation. Moreover, we also compare the results of the spectral fittings using the unobscured hot dust continua due to the starburst and AGN activities. We use the spectral profile of the dust continuum model obtained from NGC 7714 by Marshall et al. (2018) for the former continuum profile. As a result, for 91/115 sources, the latter model is fitted

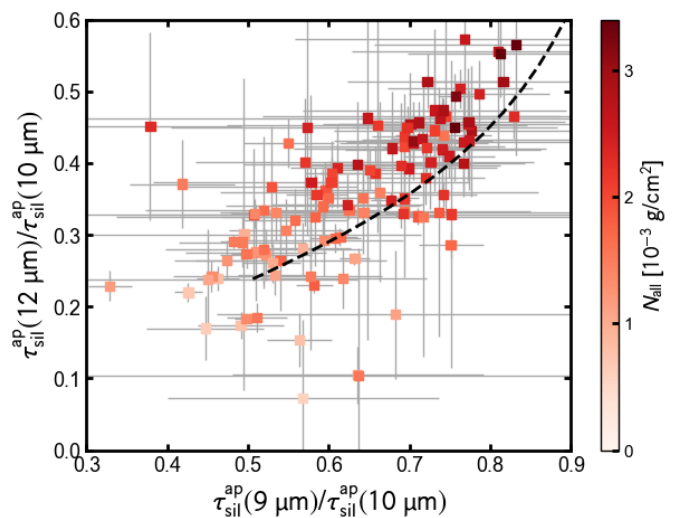


Fig. A.1. Relation between $\tau_{\text{sil}}^{\text{ap}}(12 \mu\text{m})/\tau_{\text{sil}}^{\text{ap}}(10 \mu\text{m})$ and $\tau_{\text{sil}}^{\text{ap}}(9 \mu\text{m})/\tau_{\text{sil}}^{\text{ap}}(10 \mu\text{m})$ color-coded by the total mass column density of silicate dust, N_{all} . Dashed line shows the resultant optical depth ratios obtained by the simulation of the saturation effects due to the unobscured hot dust emission.

better than the former, and, for 8/115 sources, the reduced χ^2 value improves significantly with a significance level of 5% by the F-test. Hence we conclude that the unobscured AGN component fills the 9.7 μm feature.

Appendix B: Summary of the analyses of the silicate features

The properties of silicate dust in our sample are summarized in Table B.1. Figure B.1 shows all the results of the spectral decomposition.

Table B.1. Summary of the spectral fittings.

Name (1)	N_{ol} [10^{-4} g/cm 2] (2)	N_{pyr} [10^{-5} g/cm 2] (3)	N_{cry} [10^{-6} g/cm 2] (4)	$N_{\text{pyr}}/N_{\text{all}}$ [%] (5)	$N_{\text{cry}}/N_{\text{all}}$ [%] (6)
IRAS 00091-0738	23.4 ± 0.6	14 ± 2	25.63 ± 0.08	5.2 ± 0.7	9.3 ± 0.2
IRAS F00183-7111	18.2 ± 0.2	31.9 ± 0.8	17.8 ± 0.6	13.8 ± 0.4	7.7 ± 0.3
IRAS 00188-0856	10 ± 2	0.0 ± 0.7	0.2 ± 0.6	0.0 ± 0.7	0.2 ± 0.6
IRAS 00397-1312	19.7 ± 0.5	4.0 ± 0.1	14.6 ± 0.7	1.85 ± 0.06	6.8 ± 0.4
IRAS 00406-3127	15 ± 1	0 ± 1	6 ± 1	0.0 ± 0.6	3.5 ± 0.9
IRAS 01166-0844SE	22.7 ± 0.6	49 ± 4	12.3 ± 0.1	17 ± 1	4.3 ± 0.1
IRAS F01173+1405	14.4 ± 0.1	5.0 ± 0.6	10.8 ± 0.5	3.2 ± 0.4	6.8 ± 0.3
IRAS F01197+0044	10.5 ± 0.4	0.0 ± 0.5	13 ± 1	0.0 ± 0.4	10.8 ± 0.9
IRAS 01199-2307	19.9 ± 0.4	32.7 ± 0.6	21.8 ± 0.8	12.9 ± 0.3	8.6 ± 0.3
IRAS 01298-0744	27 ± 1	14 ± 6	28.7 ± 0.8	5 ± 2	9.3 ± 0.5
IRAS 01355-1814	12.8 ± 0.2	40.4 ± 0.5	22 ± 1	21.2 ± 0.4	11.7 ± 0.6
IRAS F01478+1254	19 ± 3	5 ± 9	21 ± 2	2 ± 4	10 ± 2
IRAS 01569-2939	20.6 ± 0.4	25 ± 1	27.0 ± 0.6	9.6 ± 0.6	10.5 ± 0.3
IRAS 02438+2122	13.6 ± 0.1	0.0 ± 0.6	3.9 ± 0.2	0.0 ± 0.4	2.8 ± 0.1
IRAS 02455-2220	13.95 ± 0.07	0	8 ± 1	0	6 ± 1
IRAS 02530+0211	12.2 ± 0.4	40 ± 2	9.4 ± 0.5	23 ± 2	5.5 ± 0.3
IRAS 03158+4227	22 ± 1	0 ± 4	1.9 ± 0.4	0 ± 2	0.9 ± 0.2
NGC 1377	14.1 ± 0.1	62.7 ± 0.9	19.71 ± 0.08	28.1 ± 0.5	8.82 ± 0.07
IRAS 03538-6432	14 ± 2	0 ± 3	4 ± 3	0 ± 2	3 ± 2
IRAS 03582+6012	27.6 ± 0.5	6 ± 3	7.4 ± 0.3	2 ± 1	2.5 ± 0.1
IRAS 04074-2801	21.5 ± 0.8	13 ± 4	23.6 ± 0.8	5 ± 2	9.4 ± 0.5
IRAS 04313-1649	24.3 ± 0.9	1 ± 3	6.1 ± 0.9	0 ± 1	2.4 ± 0.4
IRAS 04384-4848	15.6 ± 0.1	0.0 ± 0.2	10 ± 1	0.0 ± 0.1	6.0 ± 0.7
ESO 203-IG001	19.6 ± 0.4	46 ± 1	35.5 ± 0.4	16.4 ± 0.5	12.8 ± 0.2
IRAS 05020-2941	22.9 ± 0.8	27 ± 3	31.1 ± 0.8	9 ± 1	10.8 ± 0.4
IRAS F06076-2139	11.0 ± 0.1	0.0 ± 0.5	0.8 ± 0.5	0.0 ± 0.4	0.8 ± 0.5
IRAS 06206-6315	12 ± 2	0 ± 4	9.2 ± 0.6	0 ± 3	7 ± 1
IRAS 06301-7934	19.8 ± 0.2	27 ± 1	24 ± 1	11.0 ± 0.4	9.7 ± 0.5
IRAS 06361-6217	12.9 ± 0.7	0	9.6 ± 0.6	0	6.9 ± 0.5
IRAS F07224+3003	17.4 ± 0.3	7 ± 1	6.3 ± 0.4	3.7 ± 0.6	3.4 ± 0.2
IRAS 07251-0248	24.2 ± 0.6	0	3.0 ± 0.5	0	1.2 ± 0.2
MCG +02-20-003	23.9 ± 0.2	0 ± 1	2.4 ± 0.4	0.0 ± 0.4	1.0 ± 0.2
SDSS J082001.72+505039.1	8 ± 2	13 ± 3	0.00 ± 0.04	14 ± 4	0.00 ± 0.04
IRAS 08201+2801	25 ± 1	5 ± 7	18.9 ± 0.8	2 ± 2	6.8 ± 0.5
IRAS F08520-6850	17.0 ± 0.3	19.3 ± 0.3	15.3 ± 0.5	9.5 ± 0.2	7.5 ± 0.3
IRAS 08572+3915	13 ± 1	0 ± 2	18.7 ± 0.4	0 ± 1	12 ± 1
IRAS 09039+0503	23 ± 1	16 ± 5	9.7 ± 0.2	7 ± 2	3.8 ± 0.2
IRAS 09539+0857	24 ± 1	5.1 ± 0.6	28.0 ± 0.4	1.9 ± 0.2	10.2 ± 0.4
IRAS F10038-3338	27.15 ± 0.09	23.5 ± 0.6	28.0 ± 0.4	7.3 ± 0.2	8.7 ± 0.1
IRAS 10091+4704	31.7 ± 0.3	8.30 ± 0.09	14 ± 2	2.44 ± 0.04	4.1 ± 0.5
IRAS F10112-0040	11 ± 1	0.0 ± 0.9	4.6 ± 0.5	0.0 ± 0.8	4.1 ± 0.6
IRAS 10173+0828	23.4 ± 0.5	0	9.1 ± 0.1	0	3.75 ± 0.09
IRAS F10237+4720	27.1 ± 0.8	43 ± 5	24 ± 3	13 ± 1	7.2 ± 0.9
IRAS 10378+1109	23.2 ± 0.8	9 ± 4	5.8 ± 0.7	4 ± 2	2.3 ± 0.3
IRAS 10485-1447	13.7 ± 0.3	0	8.2 ± 0.1	0	5.6 ± 0.1
IRAS 11028+3130	24 ± 1	5.0 ± 0.2	17 ± 2	1.9 ± 0.1	7 ± 1
IRAS 11038+3217	19.6 ± 0.4	16 ± 2	5 ± 2	7.5 ± 0.9	2.2 ± 0.9
IRAS 11095-0238	23.6 ± 0.5	7.6 ± 0.2	19.7 ± 0.5	2.91 ± 0.09	7.5 ± 0.3
IRAS 11130-2659	21 ± 1	23 ± 6	28.6 ± 0.8	9 ± 2	11.1 ± 0.7
IRAS 11180+1623	19.5 ± 0.5	35.0 ± 0.9	21 ± 1	13.9 ± 0.5	8.5 ± 0.6
IRAS 11223-1244	11.7 ± 0.6	0.0 ± 0.2	6.4 ± 0.9	0.0 ± 0.2	5.2 ± 0.8
IRAS 11506+1331	11.7 ± 0.4	0	17.7 ± 0.3	0	13.1 ± 0.5
IRAS 11524+1058	18 ± 1	0 ± 4	7 ± 2	0 ± 2	4 ± 1
IRAS 11582+3020	23.3 ± 0.2	16.0 ± 0.1	16 ± 1	6.02 ± 0.07	6.2 ± 0.5
IRAS 12032+1707	20.4 ± 0.2	0 ± 1	6.0 ± 0.7	0.0 ± 0.5	2.8 ± 0.4

Table B.1. Continued.

Name (1)	N_{ol} [10^{-4} g/cm 2] (2)	N_{pyr} [10^{-5} g/cm 2] (3)	N_{cry} [10^{-6} g/cm 2] (4)	$N_{\text{pyr}}/N_{\text{all}}$ [%] (5)	$N_{\text{cry}}/N_{\text{all}}$ [%] (6)
IRAS 12127-1412	7.71 ± 0.07	0	4.0 ± 0.2	0	4.9 ± 0.2
IRAS F12224-0624	33.2 ± 0.2	0 ± 1	7 ± 1	0.0 ± 0.4	2.1 ± 0.3
NGC 4418	20.0 ± 0.1	6.2 ± 0.9	17.0 ± 0.3	2.8 ± 0.4	7.6 ± 0.1
IRAS 12359-0725	14.0 ± 0.8	0	10.5 ± 0.9	0	7.0 ± 0.7
IRAS 12447+3721	16.0 ± 0.3	56 ± 2	17.1 ± 0.8	24 ± 1	7.3 ± 0.4
IRAS F13045+2354	9.2 ± 0.4	0	13 ± 1	0	12 ± 1
IRAS 13106-0922	27 ± 2	0 ± 11	3 ± 2	0 ± 4	1.3 ± 0.7
IRAS F13279+3401	20.0 ± 0.2	71.9 ± 0.7	28 ± 2	24.0 ± 0.3	9.3 ± 0.6
IRAS 13352+6402	13.2 ± 0.3	7.0 ± 0.2	5 ± 1	4.9 ± 0.2	4 ± 1
Mrk 273	14.8 ± 0.8	14 ± 2	9.5 ± 0.4	8 ± 1	5.5 ± 0.3
IRAS 14070+0525	25.2 ± 0.2	0 ± 1	8 ± 1	0.0 ± 0.5	3.2 ± 0.5
IRAS 14121-0126	16.1 ± 0.5	0.0 ± 0.3	3 ± 1	0.0 ± 0.2	1.6 ± 0.8
IRAS F14242+3258	13.6 ± 0.3	8.8 ± 0.2	10 ± 8	5.7 ± 0.3	7 ± 5
IRAS 14348-1447	21.0 ± 0.5	0 ± 2	7.5 ± 0.5	0 ± 1	3.5 ± 0.2
IRAS F14394+5332	16 ± 1	0 ± 3	4.2 ± 0.4	0 ± 2	2.6 ± 0.3
IRAS F14511+1406	9.4 ± 0.2	0.0 ± 0.7	2 ± 1	0.0 ± 0.7	3 ± 1
IRAS F14554+3858	13.2 ± 0.9	0 ± 2	0.0 ± 0.3	0 ± 1	0.0 ± 0.2
IRAS 15225+2350	12 ± 1	0 ± 1	5.7 ± 0.6	0 ± 1	4.5 ± 0.6
IRAS 15250+3609	25.6 ± 0.7	0 ± 4	14.5 ± 0.4	0 ± 2	5.4 ± 0.2
Arp 220	19 ± 2	20 ± 17	11.3 ± 0.4	9 ± 8	5.2 ± 0.7
FESS J160655.82+541500.7	4.2 ± 0.2	11.0 ± 0.9	6 ± 3	18 ± 2	10 ± 5
IRAS F16073+0209	6 ± 1	0.0 ± 0.4	7 ± 2	0.0 ± 0.6	11 ± 3
IRAS 16090-0139	21.3 ± 0.3	0 ± 1	8.2 ± 0.6	0.0 ± 0.6	3.7 ± 0.3
FESS J161759.22+541501.3	11.3 ± 0.4	0 ± 1	0.00 ± 0.01	0 ± 1	0.00 ± 0.01
IRAS F16156+0146	13 ± 2	14 ± 7	13.8 ± 0.9	9 ± 4	9 ± 1
IRAS F16242+2218	14.9 ± 0.7	0	7 ± 2	0	5 ± 2
IRAS F16305+4823	24 ± 1	21 ± 9	19 ± 1	7 ± 3	6.6 ± 0.6
IRAS 16300+1558	19 ± 1	17 ± 3	18.6 ± 0.8	7 ± 1	8.2 ± 0.5
IRAS 16455+4553	14 ± 2	0.0 ± 0.3	13.5 ± 0.7	0.0 ± 0.2	9 ± 1
IRAS 16468+5200W	19.9 ± 0.5	0.00 ± 0.08	9.7 ± 0.4	0.00 ± 0.04	4.7 ± 0.2
IRAS 16468+5200E	18.9 ± 0.5	0.00 ± 0.09	12.3 ± 0.6	0.00 ± 0.05	6.1 ± 0.3
NGC 6240	12.0 ± 0.3	10.2 ± 0.6	5.7 ± 0.2	7.5 ± 0.5	4.2 ± 0.2
IRAS 17044+6720	6.4 ± 0.2	0	6.6 ± 0.4	0	9.4 ± 0.6
IRAS F17028+3616	11 ± 1	38 ± 8	11 ± 2	24 ± 6	7 ± 2
IRAS 17068+4027	18.2 ± 0.4	4.8 ± 0.1	16.1 ± 0.7	2.38 ± 0.07	7.9 ± 0.4
IRAS 17208-0014	15.2 ± 0.3	16 ± 1	13.8 ± 0.4	8.9 ± 0.8	7.6 ± 0.3
IRAS 17463+5806	11.5 ± 0.5	85 ± 4	20 ± 1	39 ± 2	9.1 ± 0.7
IRAS 17540+2935	19 ± 1	0 ± 3	3.4 ± 0.7	0 ± 2	1.8 ± 0.4
IRAS 18443+7433	15.3 ± 0.5	3.7 ± 0.9	15.5 ± 0.5	2.2 ± 0.5	9.0 ± 0.4
IRAS 18531-4616	22.8 ± 0.5	1 ± 3	16 ± 2	1 ± 1	6.7 ± 0.7
IRAS 18588+3517	22.4 ± 0.3	10.4 ± 0.1	6.2 ± 0.6	4.32 ± 0.07	2.6 ± 0.3
IRAS 20087-0308	15.2 ± 0.6	0	5 ± 1	0	3.3 ± 0.7
IRAS 20100-4156	21.9 ± 0.7	0.0 ± 0.9	6.4 ± 0.6	0.0 ± 0.4	2.8 ± 0.3
IRAS 20109-3003	20.1 ± 0.4	17 ± 1	21 ± 1	7.0 ± 0.6	8.9 ± 0.4
IRAS 20286+1846	15.7 ± 0.7	0 ± 2	10 ± 2	0 ± 1	6 ± 1
IRAS 20551-4250	15.0 ± 0.4	8.1 ± 0.2	15.5 ± 0.6	4.7 ± 0.2	8.9 ± 0.4
IRAS 21077+3358	16.5 ± 0.1	0	4.1 ± 0.7	0	2.4 ± 0.4
IRAS 21272+2514	17.0 ± 0.3	0.0 ± 0.8	7 ± 1	0.0 ± 0.5	3.7 ± 0.6
IRAS F21329-2346	13 ± 1	23 ± 6	18.1 ± 0.3	13 ± 4	10.4 ± 0.8
IRAS F21541-0800	5.7 ± 0.2	11.8 ± 0.9	10.3 ± 0.7	15 ± 1	13.1 ± 0.9
NGC 7172	5.8 ± 0.2	13 ± 1	9 ± 1	17 ± 1	11 ± 1
IRAS 22088-1831W	20 ± 1	18 ± 4	23.0 ± 0.9	7 ± 2	9.3 ± 0.6
IRAS 22088-1831E	21.7 ± 0.4	19 ± 1	21 ± 1	7.3 ± 0.6	8.2 ± 0.4
IRAS 22116+0437	16.8 ± 0.2	37 ± 1	22.0 ± 0.9	16.4 ± 0.5	9.7 ± 0.4
NGC 7479	8.8 ± 0.2	16.4 ± 0.3	5.7 ± 0.5	14.9 ± 0.4	5.2 ± 0.5
IRAS 23129+2548	27.0 ± 0.9	2 ± 4	18.1 ± 0.7	1 ± 1	6.2 ± 0.3
IRAS F23234+0946	19 ± 1	9 ± 6	3.9 ± 0.2	5 ± 3	1.9 ± 0.2
IRAS 23230-6926	18.6 ± 0.5	7.8 ± 0.2	16.6 ± 0.5	3.7 ± 0.1	7.9 ± 0.3
IRAS 23253-5415	16.3 ± 0.8	0	1.7 ± 0.5	0	1.0 ± 0.3
IRAS 23365+3604	0	0 ± 12	0	0 ± 8	0

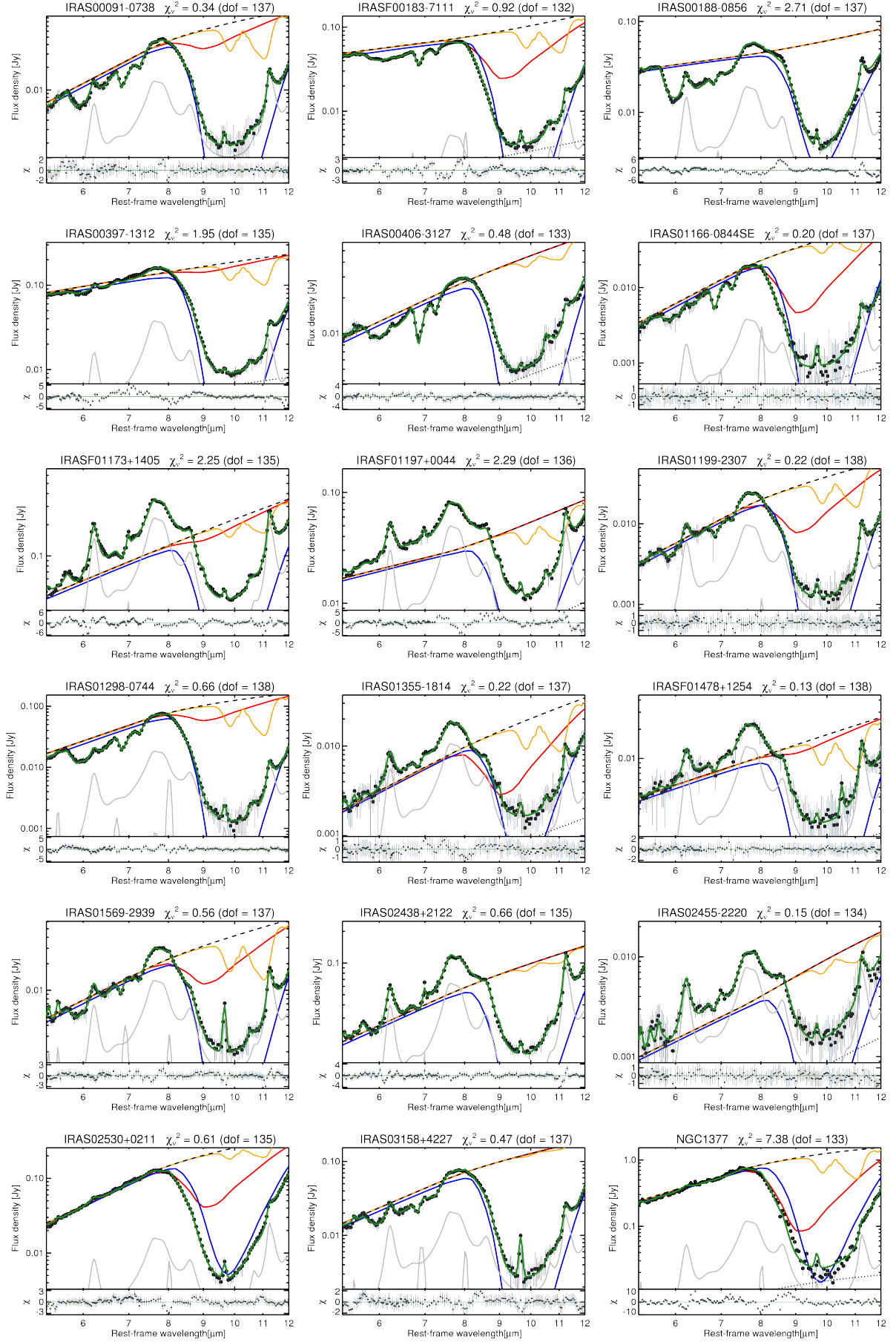


Fig. B.1. Results of the 5.3–12 μm spectral fitting for all spectra in our sample. The line colors and styles are the same as in the right panel of Fig. 1. Note that some of the components (mainly the unobscured continuum component) fall below the plotted area.

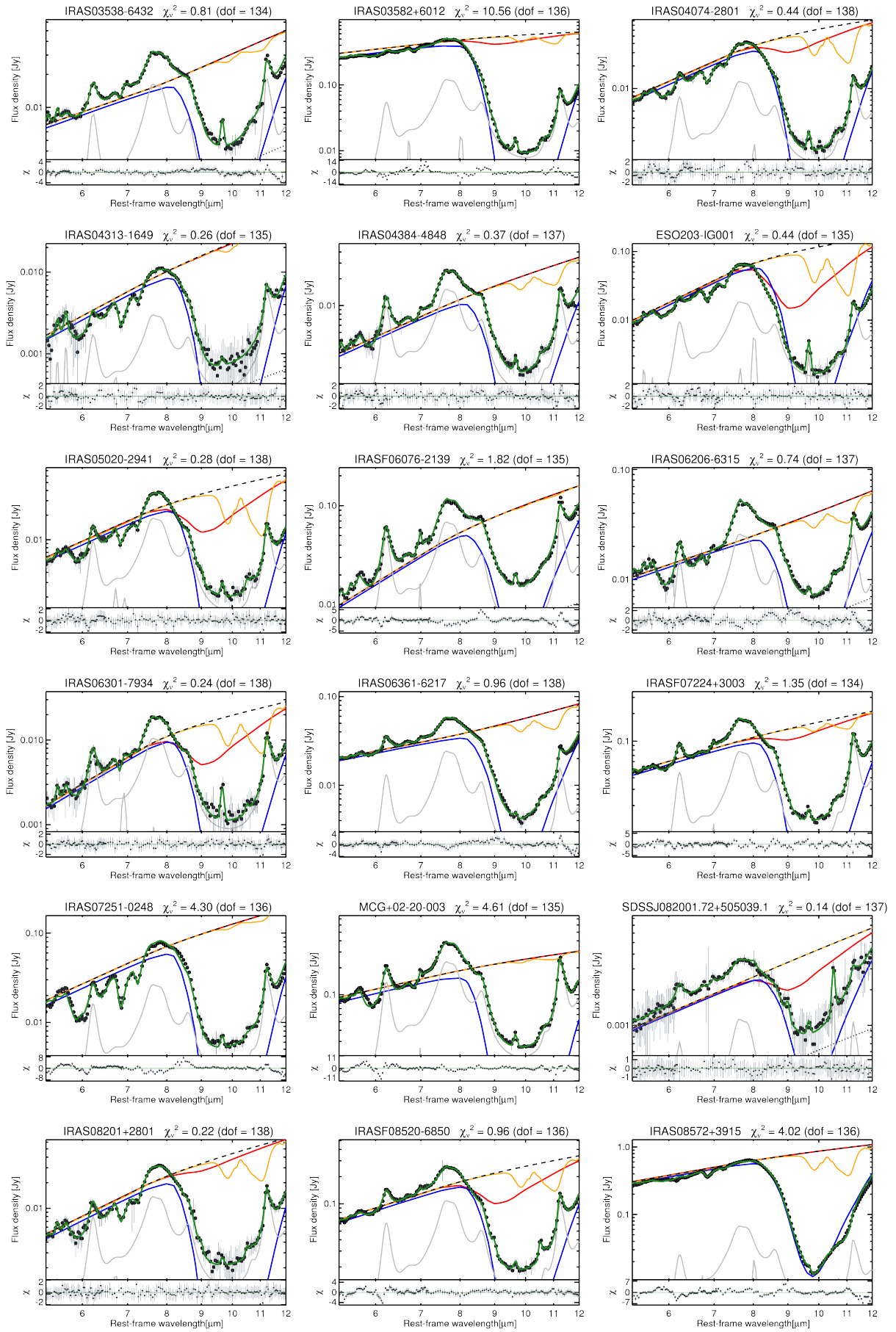


Fig. B.1. Continued.

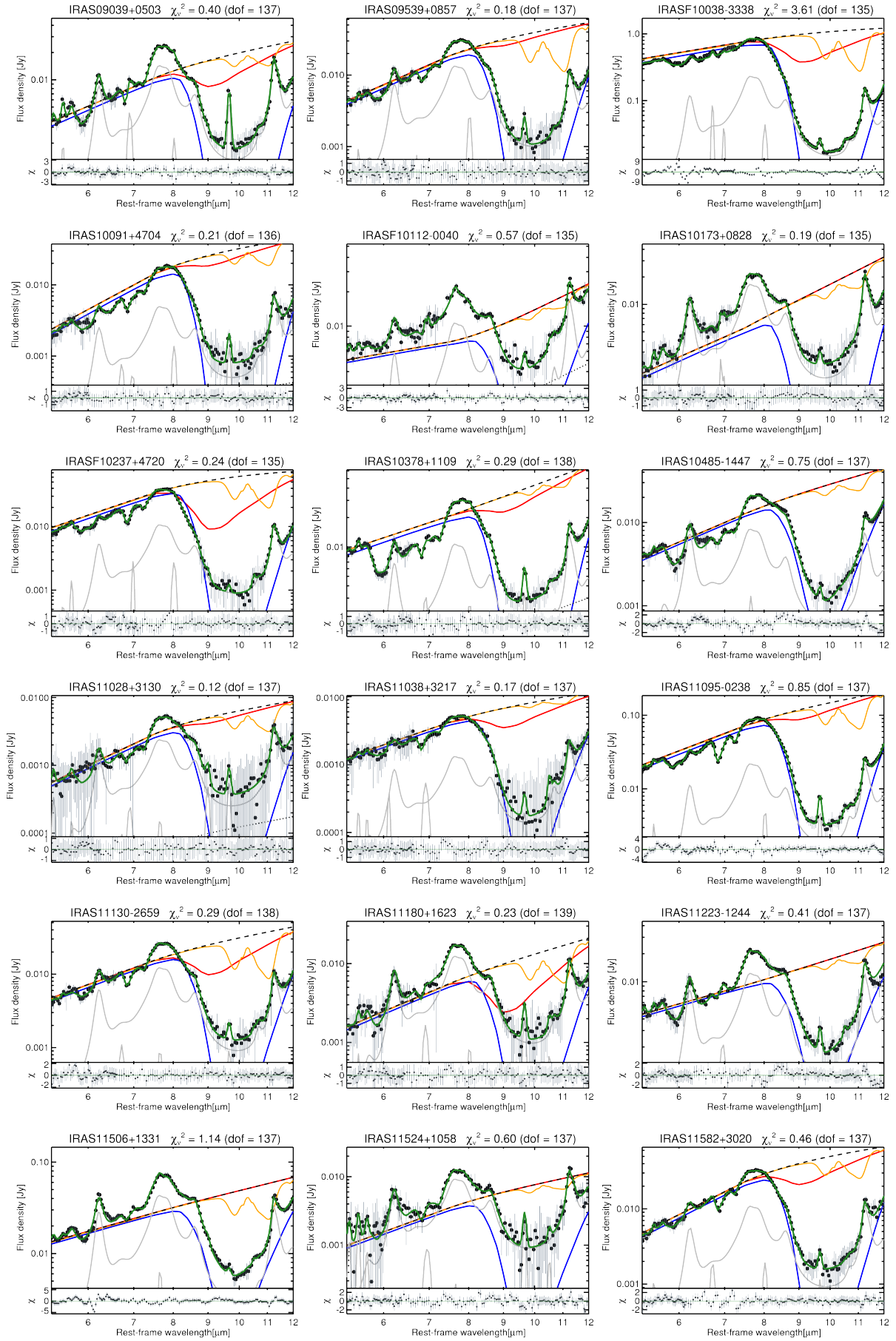


Fig. B.1. Continued.

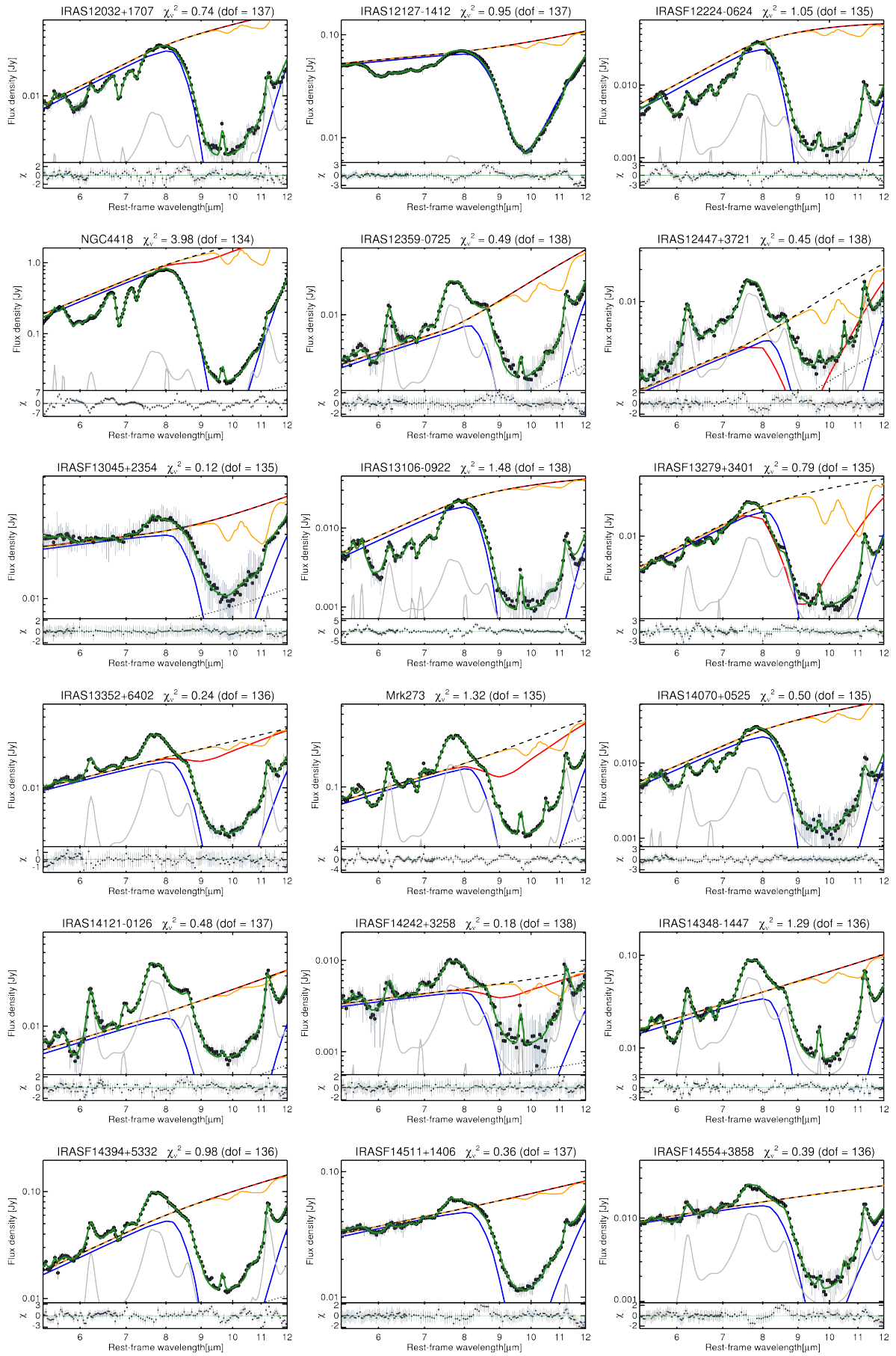


Fig. B.1. Continued.

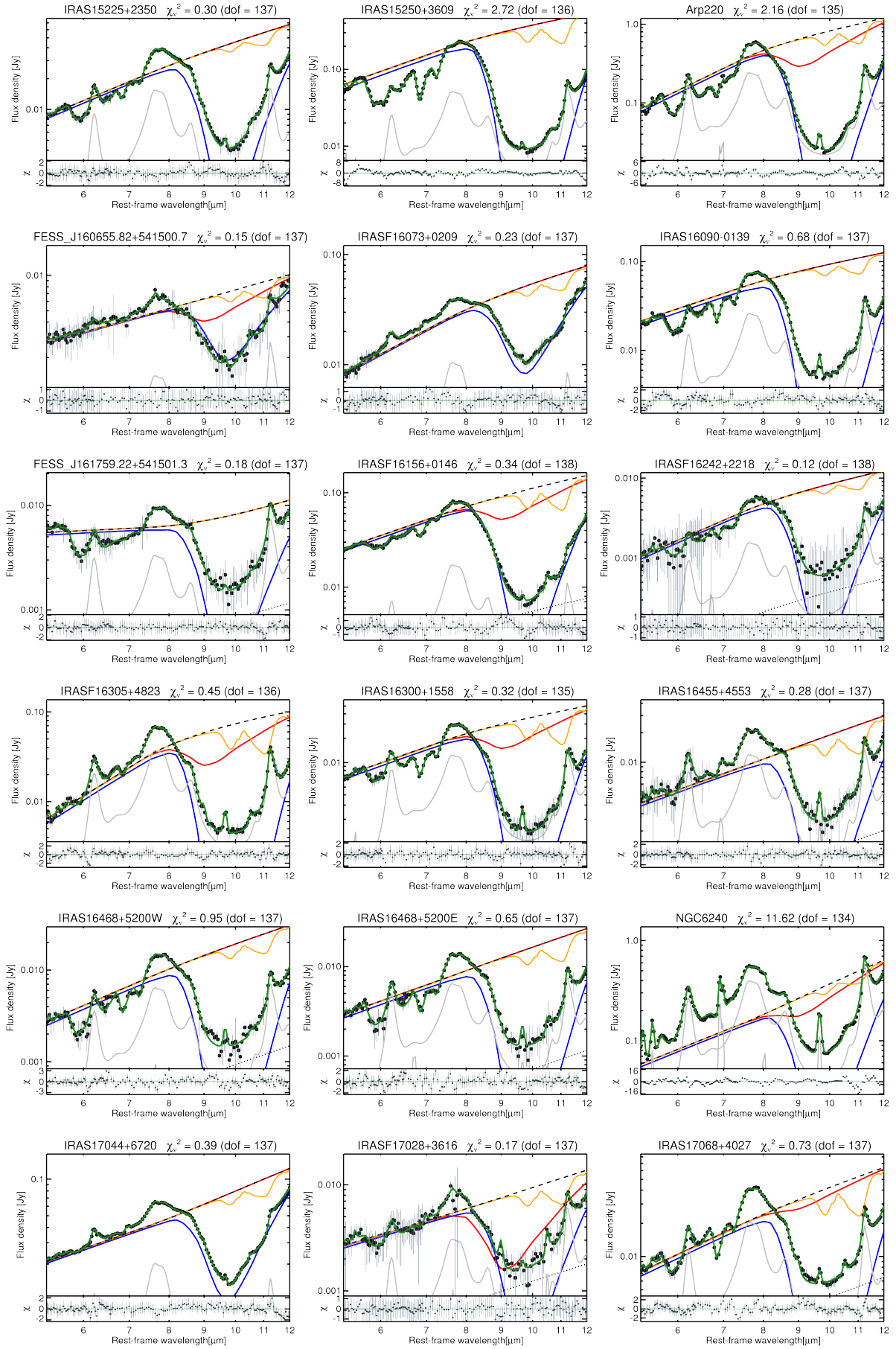


Fig. B.1. Continued.

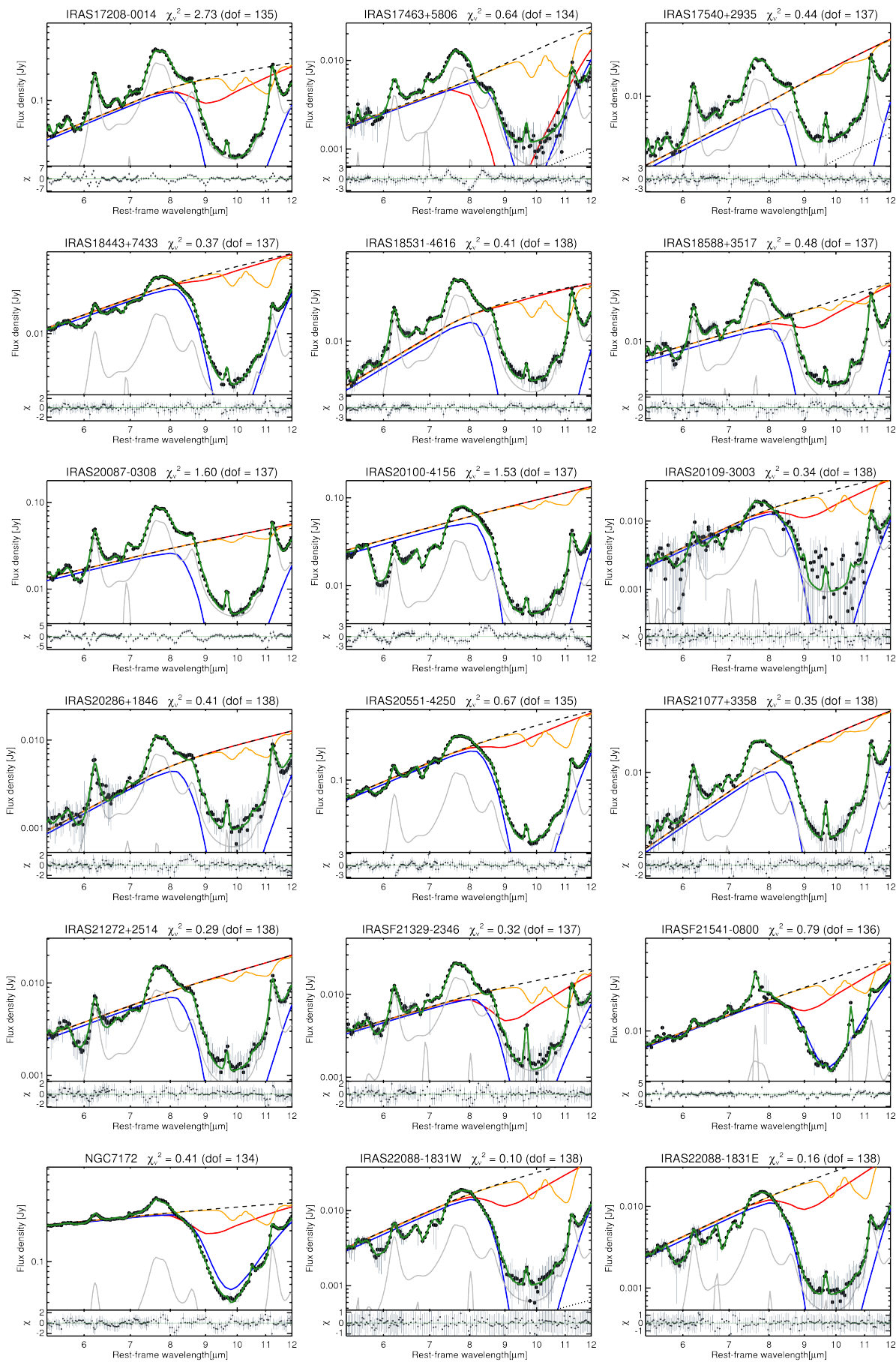


Fig. B.1. Continued.

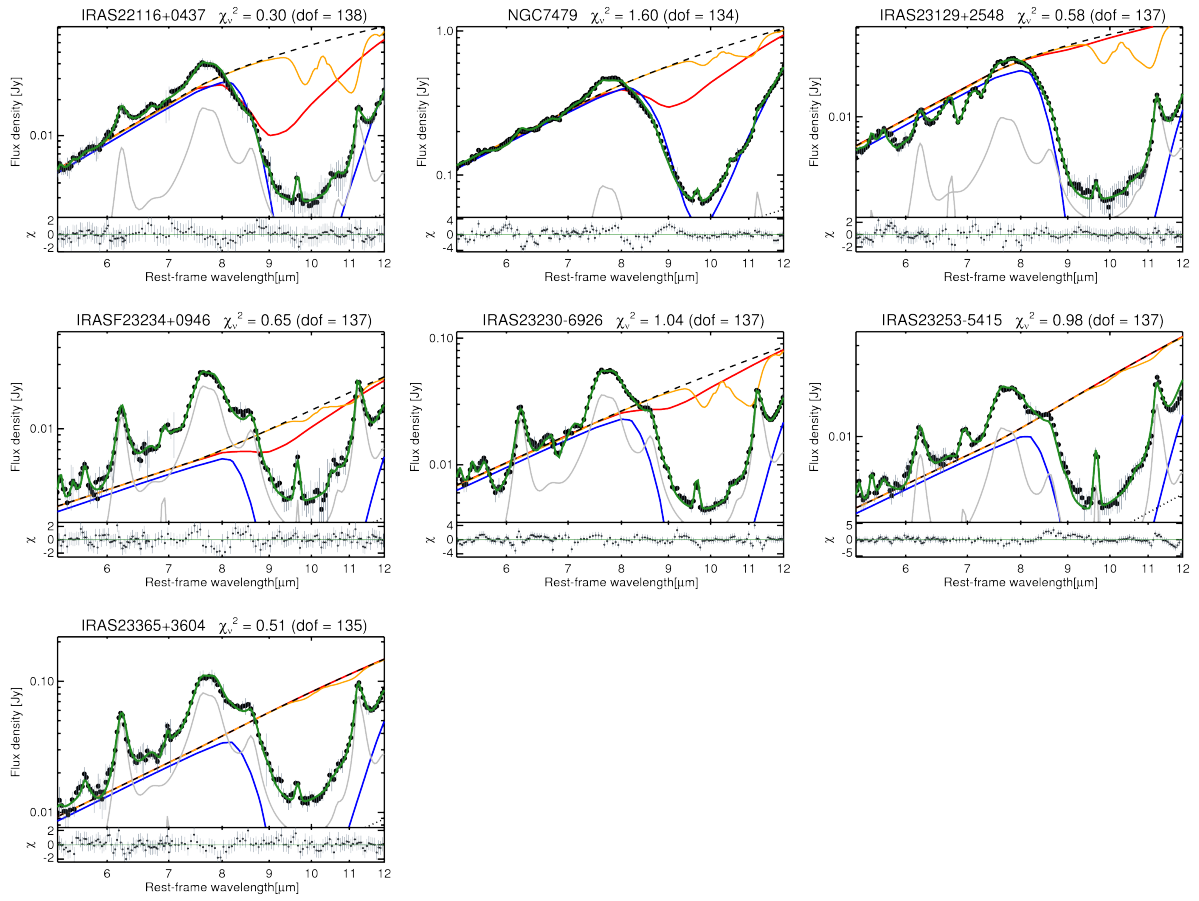


Fig. B.1. Continued.